RESEARCH ARTICLE SUMMARY

ADIPOGENIC REGULATION

Metabolic regulation of transcription through compartmentalized NAD+ biosynthesis

Keun Woo Ryu, Tulip Nandu, Jiyeon Kim, Sridevi Challa, Ralph J. DeBerardinis, W. Lee Kraus*

INTRODUCTION: Nicotinamide adenine dinucleotide (NAD) is an essential small molecule that is involved in a variety of physiological and pathological processes. The oxidized form, NAD^+, serves as a cofactor in metabolic pathways, as well as a substrate for various enzymes that consume it, such as the poly[adenosine diphosphate (ADP)–ribose] polymerases (PARPs) and sirtuins (SIRTs). PARPs and SIRTs cleave NAD^+ into nicotinamide and ADP-ribose, resulting in the irreversible breakdown of NAD^+. Therefore, the resynthesis of NAD^+ is necessary for maintaining normal cellular functions. Increasing evidence has revealed that (i) reduced NAD^+ levels result in altered metabolism and increased disease susceptibility and (ii) restoration of NAD^+ levels can prevent disease progression. Thus, understanding NAD^+ synthesis and catabolism is important for understanding physiological and pathological processes.

RATIONALE: NAD^+ is synthesized by a family of enzymes known as nicotinamide mononucleotide adenylyl transferases (NMNATs). In mammalian cells, NMNATs exhibit distinct subcellular localizations (NMNAT-1 in the nucleus, NMNAT-2 in the cytoplasm and Golgi, and NMNAT-3 in the mitochondria), suggesting that NAD^+ biosynthesis is compartmentalized within the cell. Despite the biological importance of NAD^+, the physiological role of compartmentalized NAD^+ biosynthesis in cells is largely unexplored. Given the dual role of NAD^+ as a metabolic cofactor and a substrate for enzymes involved in gene regulation, we hypothesized that compartmentalized synthesis of NAD^+ might connect cellular metabolism and gene regulation.

RESULTS: Here we show that compartment-specific NAD^+ biosynthesis acts as a key mediator of PARP-1–regulated transcription during adipocyte differentiation, integrating cellular metabolism and the adipogenic transcription program. During adipogenesis, nuclear NAD^+ levels drop concomitantly with a rapid induction of NMNAT-2, the cytoplasmic NAD^+ synthase. Increased NMNAT-2 levels limit the availability of nuclear NMN, a common substrate of NMNATs, thereby leading to a precipitous reduction in nuclear NAD^+ synthesis by NMNAT-1. This reduction of nuclear NAD^+ results in decreased PARP-1 catalytic activity, which in turn reduces inhibitory ADP-ribosylation of the adipogenic transcription factor C/EBPβ. Reduced ADP-ribosylation of C/EBPβ allows it to bind its target genes and drive a proadipogenic transcriptional program that promotes the differentiation of preadipocytes into adipocytes.

Experimentally, we found that decreasing nuclear NAD^+ synthesis by NMNAT-1 depletion significantly reduced PARP-1 enzymatic activity and enhanced adipogenesis, whereas NMNAT-2 depletion inhibited the drop in nuclear NAD^+ levels and significantly reduced adipocyte differentiation. Moreover, providing exogenous NMN to preadipocytes in culture "short-circuited" the competition between NMNAT-1 and NMNAT-2 for NMN, leading to increased nuclear NAD^+ synthesis during differentiation. This, in turn, increased PARP-1 activity and inhibited adipocyte differentiation.

Adipogenic signaling pathways and increased glucose metabolism were required for the rapid induction of NMNAT-2, and inhibition of glucose metabolism completely abolished the induction of NMNAT-2 during adipogenesis. Preventing NMNAT-2 induction by glucose deprivation restored PARP-1 activity and inhibited C/EBPβ-dependent gene expression. Collectively, these results suggest that NMNAT-1 and NMNAT-2 function as sensors to integrate cellular metabolism and the adipogenic transcription program.

CONCLUSION: We have elucidated a pathway leading from glucose uptake and metabolism, to competition between nuclear and cytoplasmic NMNATs for the NAD^+ biosynthesis precursor NMN, and ultimately to alterations in the activity of PARP-1 and its catalytic target C/EBPβ, a transcription factor that promotes adipogenic gene expression and initiates the process of adipocyte differentiation. Such mechanisms are also likely to play a key role in other biological systems that exhibit dramatic changes in nuclear PARylation as differentiation proceeds or have a high metabolic load. ∎

ON OUR WEBSITE

Read the full article at http://dx.doi.org/10.1126/science.aan5780
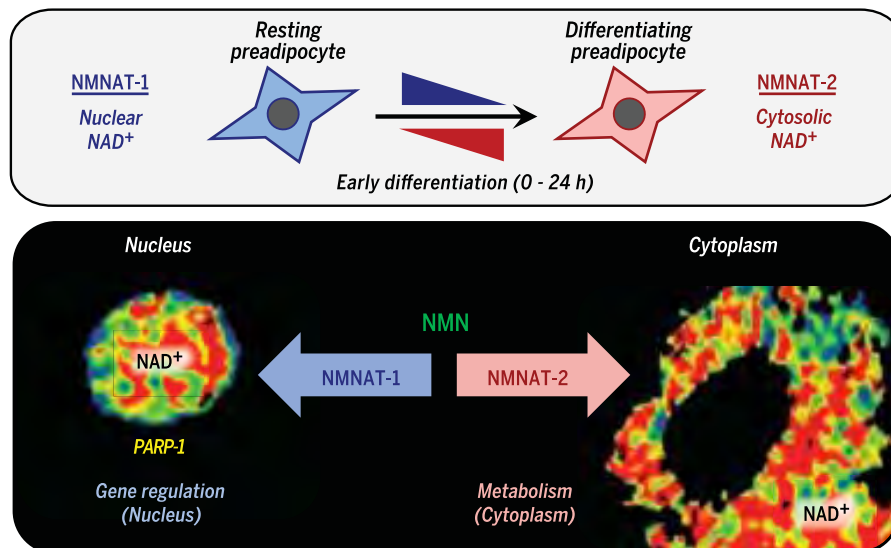
Compartmentalized NAD^+ biosynthesis by NMNATs regulates adipogenesis through PARP-1. NMNATs synthesize NAD^+ from nicotinamide mononucleotide (NMN) and adenosine triphosphate. Nuclear NMNAT-1 provides NAD^+ for nuclear ADP-ribosylation and gene regulation by PARP-1, whereas cytoplasmic NMNAT-2 provides NAD^+ for cytosolic ADP-ribosylation and cellular metabolism. Competition between NMNAT-1 and NMNAT-2 for their common substrate, NMN, promotes compartmentalized regulation of NAD^+ levels, allowing for discrete nuclear and cytoplasmic events. The fluorescent images of NAD^+ in the bottom panel were generated using a NAD^+ sensor localized to the nucleus (left) or the cytoplasm (right).

RESEARCH ARTICLE

ADIPOGENIC REGULATION

Metabolic regulation of transcription through compartmentalized NAD$^+$ biosynthesis

Keun Woo Ryu,[1,2,3] Tulip Nandu,[1,2] Jiyeon Kim,[4] Sridevi Challa,[1,2] Ralph J. DeBerardinis,[4,5,6] W. Lee Kraus[1,2,3]*

NAD$^+$ (nicotinamide adenine dinucleotide in its oxidized state) is an essential molecule for a variety of physiological processes. It is synthesized in distinct subcellular compartments by three different synthases (NMNAT-1, -2, and -3). We found that compartmentalized NAD$^+$ synthesis by NMNATs integrates glucose metabolism and adipogenic transcription during adipocyte differentiation. Adipogenic signaling rapidly induces cytoplasmic NMNAT-2, which competes with nuclear NMNAT-1 for the common substrate, nicotinamide mononucleotide, leading to a precipitous reduction in nuclear NAD$^+$ levels. This inhibits the catalytic activity of poly[adenosine diphosphate (ADP)–ribose] polymerase–1 (PARP-1), a NAD$^+$-dependent enzyme that represses adipogenic transcription by ADP-ribosylating the adipogenic transcription factor C/EBPβ. Reversal of PARP-1–mediated repression by NMNAT-2–mediated nuclear NAD$^+$ depletion in response to adipogenic signals drives adipogenesis. Thus, compartmentalized NAD$^+$ synthesis functions as an integrator of cellular metabolism and signal-dependent transcriptional programs.

Extracellular signaling and nutrient availability are major factors determining cell fate decisions (1). Biologically appropriate responses to extracellular information require alterations in cellular metabolism and the gene expression programs that control cellular outcomes (2). Many enzymes involved in gene regulation require substrates or cofactors that are products of intermediate cellular metabolism, providing a direct link between metabolism and transcription (1, 3). How cells integrate extracellular signals (e.g., hormones) and cellular metabolism to coordinate transcriptional outcomes, however, is poorly understood. Recent findings suggest that fluctuations in nuclear metabolite levels, perhaps controlled by metabolic enzymes in the nucleus, underlie the coordination of these responses (1, 3).

NAD$^+$, the oxidized form of nicotinamide adenine dinucleotide, is an essential small-molecule cofactor in metabolic redox reactions, as well as a substrate for NAD$^+$-dependent enzymes, such as the poly[adenosine diphosphate (ADP)–ribose] polymerases (PARPs) and sirtuins (SIRTs), which play important roles in gene regulation (4–7). Unlike metabolic redox reactions, which reversibly oxidize or reduce NAD$^+$, PARPs and SIRTs cleave NAD$^+$ into nicotinamide and ADP-ribose, resulting in the irreversible consumption of NAD$^+$. Thus, the resynthesis of NAD$^+$ is crucial for preserving cellular functions. In mammalian cells, NAD$^+$ is synthesized from nicotinamide mononucleotide (NMN) and adenosine triphosphate (ATP) by a family of enzymes known as NMN adenylyl transferases (NMNATs) (4, 6). NMNATs exhibit distinct and mutually exclusive subcellular localizations: NMNAT-1 localizes to the nucleus, NMNAT-2 to the cytoplasm and Golgi, and NMNAT-3 to the mitochondria (Fig. 1A), suggesting compartment-specific regulation of NAD$^+$ biosynthesis within the cell. Given the dual role of NAD$^+$ as a metabolic cofactor and a substrate for enzymes involved in gene regulation, we hypothesized that the compartmentalized synthesis of NAD$^+$ might connect cellular metabolism and gene regulation.

Nuclear NAD$^+$ synthesis regulates PARP-1 activity and adipogenesis

To test this hypothesis, we selected a biological system that requires both dynamic transcriptional regulation and active cellular metabolism, namely, adipogenesis. Adipose tissue is an important regulator of energy balance and glucose homeostasis (8). The formation of functional adipocytes is achieved by the differentiation of preadipocytes into mature adipocytes (i.e., adipogenesis), which is tightly controlled by the sequential expression of key adipogenic transcription factors (9, 10), as well as a diverse range of metabolic pathways (1, 11). Chemical inhibition (with FK866) or depletion [with short hairpin RNA (shRNA)–mediated knockdown] of nicotinamide phosphoribosyltransferase (NAMPT), a key enzyme in NAD$^+$ biosynthesis that produces NMN (12), has been previously shown to promote adipogenesis in mesenchymal stem cells (13), suggesting a potential role of NAD$^+$ biosynthesis in adipocyte differentiation.

To explore the role of compartmentalized NAD$^+$ synthesis during adipogenesis, we first assayed the expression of NMNAT mRNAs in adipose tissue and preadipocytes. We found that NMNAT-1 and NMNAT-2 are expressed in adipose tissue and preadipocytes (fig. S1, A and B), whereas NMNAT-3 is expressed at very low to undetectable levels in preadipocytes (fig. S1B), suggesting potential cross-talk between the nuclear and cytoplasmic NAD$^+$ biosynthesis pathways during adipogenesis. We recently reported on the dynamic regulation of PARP-1 enzymatic activity during adipogenesis (14) (figs. S2A, S3A, and S3B), suggesting a role for nuclear NAD$^+$ during adipocyte differentiation.

To determine the effects of nuclear NAD$^+$ biosynthesis on adipogenesis, we used shRNA-mediated knockdown of Nmnat1 in 3T3-L1 preadipocytes (15), a versatile and well-characterized cell line. Depletion of NMNAT-1 dramatically reduced PARP-1 enzymatic activity, as determined by blotting for poly(ADP-ribose) (PAR), which continued to decrease during the early phase (the first 24 hours) of differentiation (Fig. 1B and fig. S2A). PARP-1 activity in NMNAT-1–depleted cells was restored by re-expression of catalytically active, but not inactive, NMNAT-1, suggesting that nuclear NAD$^+$ synthesis is required for PARP-1 activity (fig. S2B). Depletion of NMNAT-1 had a much greater effect on the activity of PARP-1 than on that of SIRT1, a nuclear NAD$^+$-dependent protein deacetylase (fig. S3, C to F), likely owing to the abundant expression of PARP-1 in preadipocytes (fig. S3G). Previously, we showed that inhibition of PARP-1 enzymatic activity during the early phase of adipogenesis in 3T3-L1 cells enhances differentiation (14). Depletion of NMNAT-1 phenocopies depletion of PARP-1; it increases lipid accumulation (Fig. 1, C and D), induces the expression of adipocyte marker genes (e.g., Fabp4 and Adipoq), and induces the expression of transcription factors that promote terminal differentiation and maintain adipocyte function (e.g., PPARγ and C/EBPα) (Fig. 2A and fig. S4A). Similar effects on bulk PARP-1–mediated PARylation and the expression of adipocyte marker genes were observed in response to Nmnat1 knockdown in NIH 3T3 cells (fig. S4, B and C), as well as in response to Nmnat1 knockout in primary preadipocytes from the stromal-vascular fraction (SVF) of adipose tissue collected from mice (16, 17) (fig. S4, D to F). Together, these results link the proadipogenic phenotype observed upon NMNAT-1 depletion to decreased PARP-1 activity in three different models of adipogenesis.

[1]Laboratory of Signaling and Gene Regulation, Cecil H. and Ida Green Center for Reproductive Biology Sciences, University of Texas Southwestern Medical Center, Dallas, TX 75390, USA. [2]Division of Basic Research, Department of Obstetrics and Gynecology, University of Texas Southwestern Medical Center, Dallas, TX 75390, USA. [3]Program in Genetics, Development, and Disease, Graduate School of Biomedical Sciences, University of Texas Southwestern Medical Center, Dallas, TX 75390, USA. [4]Children's Medical Center Research Institute, University of Texas Southwestern Medical Center, Dallas, TX 75390, USA. [5]Department of Pediatrics, University of Texas Southwestern Medical Center, Dallas, TX 75390, USA. [6]McDermott Center for Human Growth and Development, University of Texas Southwestern Medical Center, Dallas, TX 75390, USA.
*Corresponding author. Email: lee.kraus@utsouthwestern.edu

NMNAT-1 and PARP-1 control adipogenic gene expression through C/EBPβ

In follow-up experiments, we performed RNA sequencing (RNA-seq) using *Nmnat1* or *Parp1* knockdown in 3T3-L1 cells to confirm that enhanced differentiation in response to reduced nuclear NAD⁺ synthesis occurs through PARP-1. At 2 days postdifferentiation, we observed significant overlap between the genes whose expression was altered upon *Nmnat1* or *Parp1* knockdown (Fig. 2B), further supporting the conclusion that NMNAT-1 regulates differentiation through PARP-1. To elucidate potential mechanisms underlying NMNAT-1– and PARP-1–dependent transcriptional regulation during adipogenesis, we determined which adipogenic transcription factor binding sites (presumed enhancers) interact with the promoters of NMNAT-1 and PARP-1–co-regulated genes in 3T3-L1 cells by integrating promoter capture Hi-C (PCHI-C) data with transcription factor chromatin immunoprecipitation (ChIP)–seq data (*18*, *19*). Greater than 70% of the promoters of the co-regulated genes looped to binding sites for C/EBPβ, a key adipogenic transcription factor during the early phase of adipocyte differentiation (*9*, *10*) (Fig. 2C and fig. S5, A to C). Together, these results implicate C/EBPβ in the expression of adipogenic genes upon NMNAT-1 and PARP-1 depletion, leading to enhanced adipocyte differentiation. Importantly, C/EBPβ expression was not altered upon *Nmnat1* knockdown in 3T3-L1 cells, either at the mRNA or protein level (Fig. 2, D and E), suggesting that enhanced differentiation was not due to increased expression of C/EBPβ. We have recently shown that PARP-1 PARylates C/EBPβ during the early phase of adipogenesis, thereby inhibiting its DNA-binding ability (*14*). Indeed, depletion of NMNAT-1 significantly increased C/EBPβ binding to target gene promoters, as assessed by ChIP–quantitative

real-time polymerase chain reaction (qPCR) (Fig. 2F). In addition, the genes whose promoters interact with known C/EBPβ binding sites were significantly induced upon depletion of NMNAT-1 or PARP-1 (Fig. 2G and fig. S5D). These results demonstrate that nuclear NAD⁺ synthesis by NMNAT-1 regulates PARP-1 enzymatic activity, which in turn modulates the adipogenic transcription program by regulating the binding of C/EBPβ to its target genes.

Increases in cytoplasmic NAD⁺ synthesis by NMNAT-2 reduces nuclear NAD⁺ levels

Because PAR levels rapidly decrease during differentiation (Fig. 3A and fig. S2A) and nuclear NAD⁺ synthesis is required for PARP-1 enzymatic activity, we hypothesized that NAD⁺ levels may decrease during the early phase of adipogenesis. Unexpectedly, however, the total intracellular NAD⁺ levels did not change during differentiation (Fig. 3A). We then postulated that nuclear NAD⁺ could be regulated differently from total intracellular NAD⁺. To test this hypothesis, we used NAD⁺ biosensors that contain a bipartite NAD⁺-binding domain from a bacterial NAD⁺-dependent DNA ligase fused to cpVenus fluorescent protein, with either nuclear or cytoplasmic localization signals (*20*) (Fig. 3B, top). These nuclear and cytoplasmic NAD⁺ sensors exhibited reduced fluorescence upon the binding of NAD⁺ (fig. S6, A to C). We expressed either the nuclear or cytoplasmic sensor and a corresponding cpVenus-only control in 3T3-L1 cells. We then generated a dose-response curve by normalizing the external NAD⁺ concentration and permeabilizing the cells with digitonin (*20*). As previously reported, NAD⁺ decreased the fluorescent signal from the sensors in a dose-dependent manner but had no effect on the cpVenus-only control

(*20*) (fig. S6, D and E). When treated with FK866, an inhibitor of NAMPT that depletes intracellular NAD⁺ in all subcellular compartments, both the nuclear and cytoplasmic NAD⁺ sensors exhibited a strong increase in NAD⁺ sensor fluorescence owing to loss of NAD⁺ binding (fig. S6, F to J). Thus, these sensors are capable of measuring changes in subcellular NAD⁺ levels. Using the dose-response curve generated by NAD⁺ permeabilization (fig. S6E), we estimated subcellular NAD⁺ concentrations to be ~100 μM in both the nucleus and the cytoplasm, consistent with previous observations in human embryonic kidney 293T and HeLa cells (*20*).

Using 3T3-L1 cells expressing the nuclear NAD⁺ sensor, we observed an increase in the sensor signal during the early phase of differentiation, indicating a decrease in nuclear NAD⁺ levels (Fig. 3, B and C, left, and fig. S7A). This decrease in nuclear NAD⁺ levels occurred concurrently with a decrease in PARP-1 enzymatic activity (Fig. 3A and figs. S2A and S3A). At 8 hours postdifferentiation, the estimated nuclear NAD⁺ concentration was near 40 μM—well below PARP-1's Michaelis constant (K_m) for NAD⁺ [~85 to 110 μM (*21*)]—indicating that decreases in nuclear NAD⁺ levels have the potential to regulate PARP-1 enzymatic activity during differentiation.

Given the observed decrease in nuclear NAD⁺ levels without a change in total intracellular NAD⁺ levels, we hypothesized that NAD⁺ levels in another subcellular compartment might be altered differently from those in the nuclear compartment. In this regard, we observed that the levels of mRNA and protein for the cytosolic NAD⁺ synthase, NMNAT-2, were rapidly induced within 8 hours of differentiation (Fig. 3A and figs. S8, S9A, and S9B). These changes in NMNAT-2 mRNA and protein were accompanied by increased levels of cytoplasmic NAD⁺
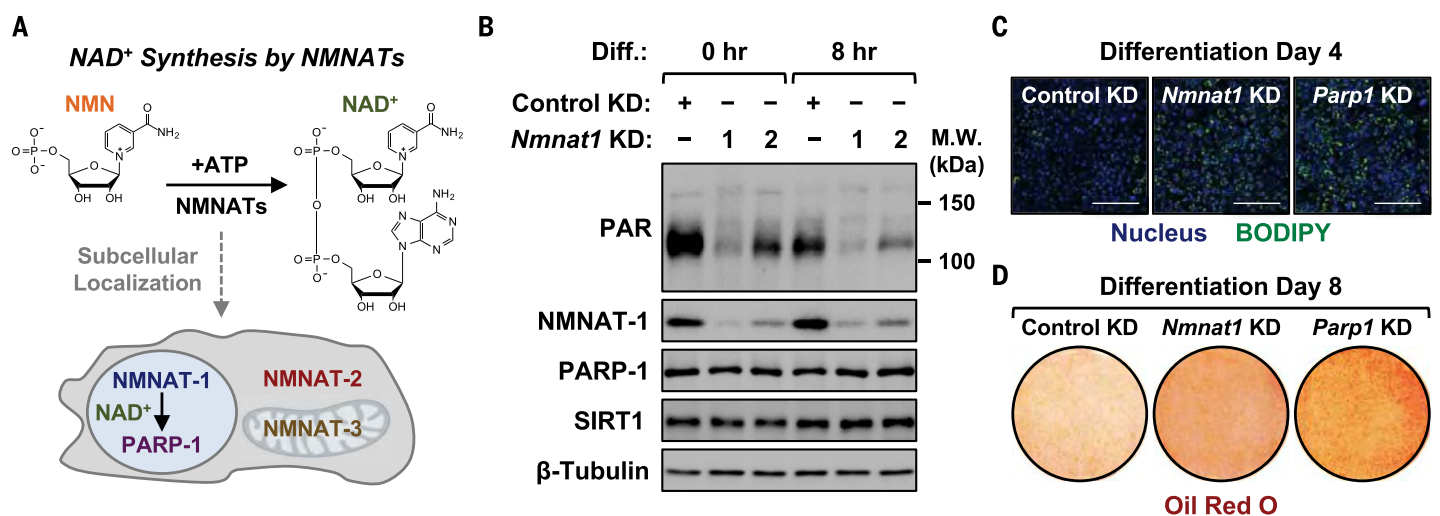
Fig. 1. NMNAT-1 regulates PARP-1 activity and adipocyte differentiation. (**A**) Schematic representation of NAD⁺ biosynthesis by NMNATs and their subcellular localization. (**B**) Western blot showing the levels of PAR upon shRNA-mediated knockdown (KD) of *Nmnat1* during the early phase of adipogenesis in 3T3-L1 cells. PAR levels (primarily automodification of PARP-1) represent the enzymatic activity of PARP-1. Blots of NMNAT-1, PARP-1, and SIRT1 are shown for comparison (β-tubulin was used as a control). M.W., molecular weight. (**C** and **D**) Accumulation of lipid droplets at 4 days (C) and 8 days (D) of differentiation after knockdown of *Nmnat1* or *Parp1* in 3T3-L1 cells. Lipids were stained using BODIPY 493/503 [green, (C)] or Oil Red O [red, (D)], and nuclei were stained using TO-PRO-3 [blue, (C)]. Scale bars in (C), 150 μm.

during differentiation (Fig. 3, B and C), suggesting that a rapid induction of cytoplasmic NAD$^+$ synthesis may lead to compartmentalized regulation of NAD$^+$. To determine whether the rapid induction of NMNAT-2 might be responsible for the concomitant reduction in nuclear NAD$^+$ levels, we measured nuclear NAD$^+$ levels upon *Nmnat2* knockdown. Unexpectedly, depletion of NMNAT-2 (fig. S9, A and B) blocked the reduction in nuclear NAD$^+$ levels during differentiation (Fig. 3, D and E, and fig. S7B), suggesting that increased cytoplasmic NAD$^+$ synthesis may control nuclear NAD$^+$ levels. Moreover, depletion of NMNAT-2 increased nuclear PARP-1 enzymatic activity (fig. S9B) and inhibited adipogenesis, as determined by the expression of adipogenic marker genes (Fig. 3F), without altering the total intra-

cellular NAD$^+$ levels (fig. S9C). We further tested whether NMNAT-2 induction was sufficient to regulate PARP-1 activity by using 3T3-L1 cells expressing doxycycline (Dox)–inducible NMNAT-2. Nuclear PARP-1–mediated PARylation was significantly decreased in cells expressing wild-type NMNAT-2 but not in cells expressing a catalytically dead NMNAT-2 mutant (fig. S9D). Collectively, these data indicate that NMNAT-2–mediated cytoplasmic NAD$^+$ synthesis inhibits the enzymatic activity of PARP-1.

Competition for NMN regulates nuclear NAD$^+$ levels during adipocyte differentiation

How might the induction of cytoplasmic NAD$^+$ synthesis inhibit nuclear NAD$^+$ synthesis and

other nuclear events? One explanation is that NMNAT-2 competes with NMNAT-1 for their common substrates, NMN or ATP, thereby limiting substrate availability in the nucleus for NMNAT-1. In cells, the concentration of NMN is considerably lower than that of ATP (*22*), and the NMNATs have K_m values for ATP that are significantly lower than the intracellular ATP concentration (*12*). Moreover, NMN is thought to be the rate-limiting factor for NAD$^+$ biosynthesis (*4*, *12*). Therefore, we hypothesized that a rapid induction of NMNAT-2 would deplete NMN from the nucleus and decrease the nuclear NAD$^+$ concentration during differentiation (Fig. 4A). To test this hypothesis, we provided an exogenous source of NMN to 3T3-L1 cells in the culture medium. Consistent with a previous report (*23*), NMN supplementation
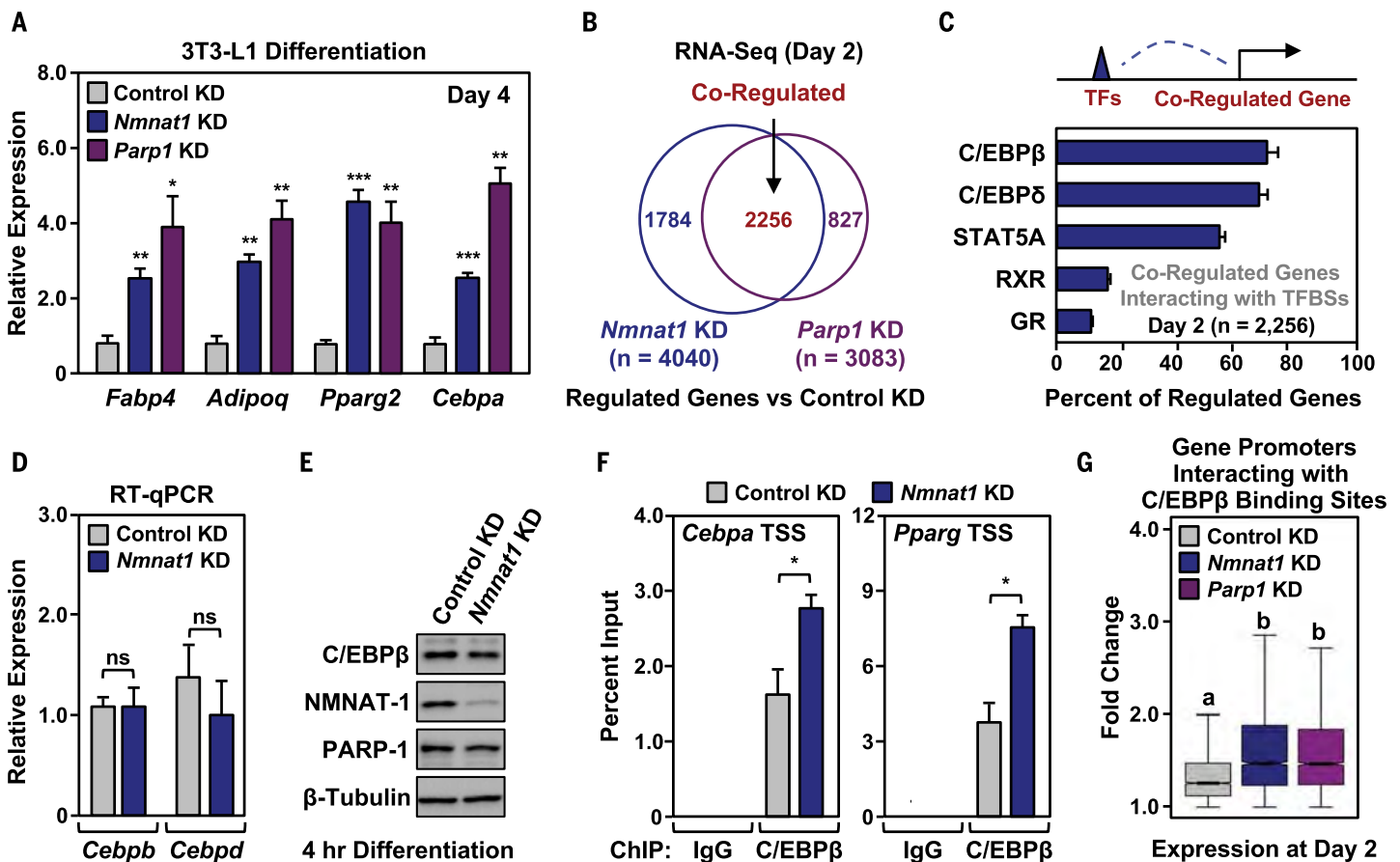
Fig. 2. NMNAT-1 and PARP-1 regulate the adipogenic transcriptional program through C/EBPβ. (**A**) Expression of adipocyte marker genes in 3T3-L1 cells at 4 days of differentiation, as determined by RT-qPCR. Each bar represents the mean + SEM (*n* = 3). Asterisks indicate significant differences from the corresponding control (Student's *t* test; *P < 0.05, **P < 0.01, ***P < 0.001). (**B**) RNA-seq assay of genes regulated upon *Nmnat1* or *Parp1* knockdown in 3T3-L1 cells compared with control knockdown after 2 days of differentiation. The overlapping region of the Venn diagram indicates co-regulated genes. (**C**) Percent of promoters of NMNAT-1 and PARP-1–co-regulated genes [from (B)] that interact with binding sites for adipogenic transcription factors (TFs). The interaction between the promoter regions of the co-regulated genes and the transcription factor binding sites (TFBSs) were determined by integrating published PCHi-C data [National Center for Biotechnology Information (NCBI) Gene Expression Omnibus (GEO) data set GSE95533] and ChIP-seq data (NCBI GEO data set GSE27826). Bars show means + SEM. (**D** and **E**) Levels of

Cebpb mRNA assessed by RT-qPCR (D) and C/EBPβ protein assessed by Western blotting (E) in 3T3-L1 cells after knockdown of *Nmnat1*. Each bar represents the mean + SEM (*n* = 3). ns, not significant (Student's *t* test; *P* > 0.05). (**F**) C/EBPβ binding at the *Cebpa* and *Pparg* gene promoters in 3T3-L1 cells after 4 hours of differentiation, as determined by ChIP-qPCR assays. Each bar represents the mean + SEM (*n* = 3). Bars marked with asterisks are significantly different from the control (Student's *t* test; *P < 0.05). (**G**) Expression of genes whose promoters interact with C/EBPβ binding sites upon knockdown of *Nmnat1* or *Parp1*. Significant C/EBPβ ChIP-seq peaks at 4 hours postdifferentiation were compared with PCHi-C–determined looping events to define the interactions. The expression level of those genes after 2 days of differentiation was compared with the expression level in control knockdown cells at day 0 to determine the fold change. Up-regulated genes (fold change > 1) were used in the analysis. Bars marked with different letters are significantly different from each other (Wilcoxon rank sum test; *P* < 0.0001).
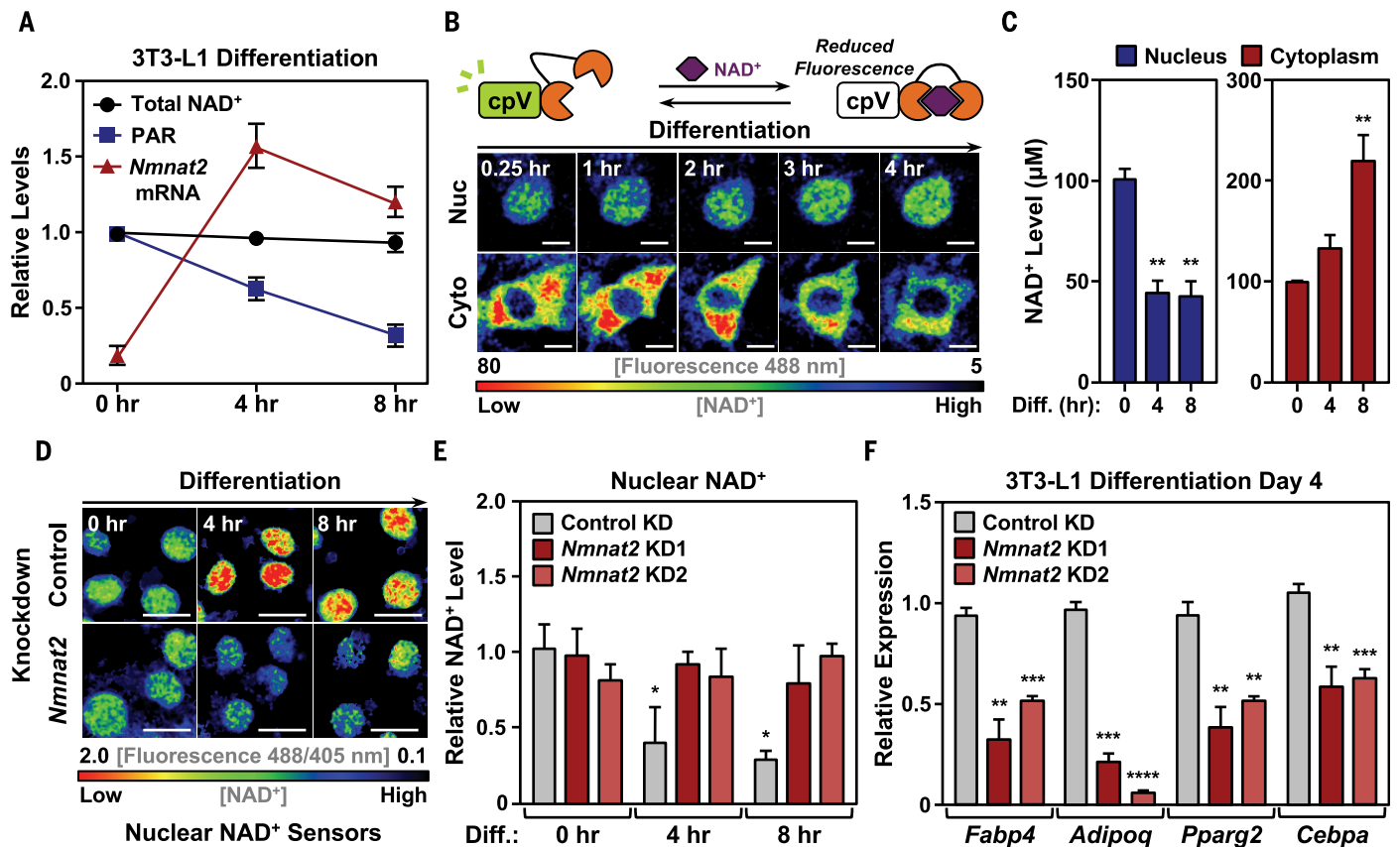
increased the total intracellular NAD⁺ levels (Fig. 4B). NMN supplementation blocked the depletion of nuclear NAD⁺ during differentiation (Fig. 4, C and D, and fig. S7C), which resulted in increased PARP-1 enzymatic activity (Fig. 4E). Supplementation with NMN also inhibited the reduction of PARP-1 activity upon ectopic expression of NMNAT-2 (fig. S9E). These results suggest that NMN availability in the nucleus dictates the extent of nuclear NAD⁺ biosynthesis. Furthermore, promoting elevated nuclear NAD⁺ levels with NMN supplementation inhibits adipogenesis in both 3T3-L1 cells and primary SVF preadipocytes, as determined by the expression of adipogenic marker genes (Fig. 4F). Thus, high nuclear NAD⁺ levels act as an inhibitory signal for adipocyte differentiation by regulating PARP-1 activity. The inhibitory effect of NMN supplementation on adipocyte differentiation was abolished upon knockdown of either *Nmnat1* or *Parp1* (Fig. 4G), and induction of

NMNAT-2 expression did not restore PARP-1 enzymatic activity after *Nmnat1* knockdown (fig. S10), further supporting our conclusion that nuclear NAD⁺ synthesis regulates adipocyte differentiation.

NMNAT-2 induction is associated with enhanced glucose metabolism

To understand why cells would require increased cytoplasmic NAD⁺ synthesis to regulate nuclear events during differentiation, we considered the role of NAD⁺ as a metabolic cofactor (Fig. 5A). During differentiation, we observed a rapid induction of key genes involved in glucose metabolism within 8 hours of differentiation, indicating increased glucose metabolism during the early phase of adipogenesis (fig. S11A). To confirm these results, we differentiated 3T3-L1 cells in medium containing D[U-¹³C]glucose (U, uniformly labeled) and measured ¹³C enrichment in intracellular metabolites by mass spectrometry (fig. S11B). We

observed a rapid (within 8 hours) increase in glycolytic intermediate metabolites containing glucose-derived ¹³C, as well as citrate m+2 (citrate containing two additional mass units from ¹³C) upon differentiation (fig. S11, C and D), indicating an increase in glucose flux into glycolysis and the tricarboxylic acid (TCA) cycle during the early phase of adipogenesis. Depletion of NMNAT-2, however, did not affect the expression of genes involved in glucose metabolism (Fig. 5B and fig. S12A). We hypothesized that elevated NMNAT-2 levels might support increased glucose metabolism during differentiation by providing a supply of cytoplasmic NAD⁺. Changes in cytoplasmic NAD⁺ concentrations could potentially affect the kinetics of the enzymes involved in glucose metabolism (fig. S12B). Indeed, *Nmnat2* knockdown decreased cytoplasmic NAD⁺ levels (fig. S12, C and D), as well as lactate secretion (fig. S12E) and the levels of glucose-derived citrate m+2

Fig. 3. Nuclear NAD⁺ levels are regulated through compartmentalized biosynthesis. (**A**) The levels of total intracellular NAD⁺ (enzyme-linked NAD⁺ assay), PAR (Western blot), and *Nmnat2* mRNA (RT-qPCR) were determined at the indicated differentiation time points in 3T3-L1 cells (means ± SEM). (**B**) Detection of nuclear (Nuc) and cytoplasmic (Cyto) NAD⁺ levels in 3T3-L1 cells by using a cpVenus-based NAD⁺ biosensor. Representative images of NAD⁺ sensor fluorescence during the early phase of differentiation are shown. (**C**) Changes in subcellular NAD⁺ levels during the early phase of differentiation of 3T3-L1 cells. NAD⁺ levels were calculated from sensor(488/405 nm)/control(488/405 nm) fluorescence ratios determined by flow cytometry using a standard curve. Each bar represents the mean + SEM (*n* = 7). Bars marked with asterisks are significantly different from the undifferentiated (0 hours) control [analysis

of variance (ANOVA); **P < 0.01]. (**D**) Representative images of nuclear NAD⁺ sensor fluorescence (488/405 nm) during differentiation upon *Nmnat2* knockdown. (**E**) Effect of *Nmnat2* knockdown on nuclear NAD⁺ levels in 3T3-L1 cells. Relative nuclear NAD⁺ levels were determined from the sensor(488/405 nm)/control(488/405 nm) fluorescence ratio using flow cytometry. Each bar represents the mean + SEM (*n* = 3). Asterisks indicate significant differences from the control knockdown at the 0-hour time point (ANOVA; *P < 0.05). (**F**) Effect of *Nmnat2* knockdown on the differentiation of 3T3-L1 cells. Differentiation was assessed by the expression of adipocyte marker genes. Each bar represents the mean + SEM (*n* = 3). Asterisks indicate significant differences from the control (Student's *t* test; **P < 0.01, ***P < 0.001; ****P < 0.0001). Scale bars, 10 μm in (B) and 20 μm in (D).

(Fig. 5C and fig. S12F). However, *Nmnat2* knockdown did not reduce the glucose flux back to basal levels (Fig. 5C and fig. S12, E and F), suggesting that induction of NMNAT-2 is not solely driving the enhanced glucose metabolism during differentiation, but rather supports glucose metabolism by supplying cytoplasmic NAD+.

We explored further whether the elevated levels of NMNAT-2 are dependent on changes in glucose flux by altering glucose levels in the differentiation medium. Unexpectedly, the induction of NMNAT-2 was abolished when 3T3-L1 cells were differentiated in medium containing low levels of glucose (Fig. 5D). PAR levels re-

mained high during differentiation with glucose deprivation (Fig. 5D), suggesting that the absence of NMNAT-2 induction leads to sustained levels of nuclear NAD+ and PARP-1 enzymatic activity. Similar results were observed when the cells were differentiated in the presence of glycolysis inhibitor 2-deoxyglucose, supporting the
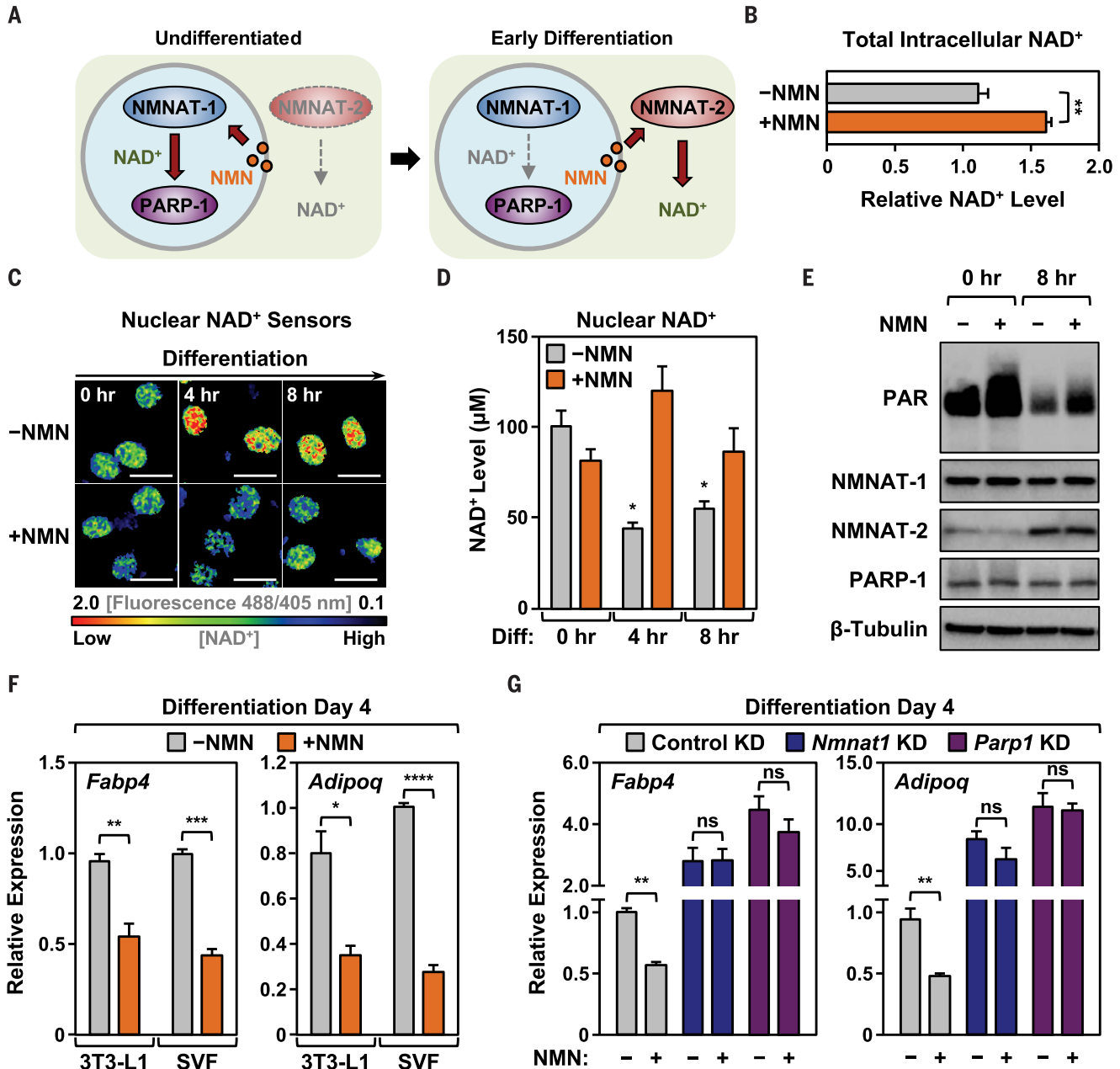
Fig. 4. Substrate competition between NMNAT-1 and NMNAT-2 regulates nuclear NAD+ levels during differentiation. (**A**) Schematic representation of substrate competition between NMNAT-1 and NMNAT-2. (**B** to **D**) Supplementation with exogenous NMN disrupts NMNAT-1 and NMNAT-2 substrate competition. Effects on total intracellular NAD+ (B) and nuclear NAD+ levels [(C) and (D)] upon supplementation with 1 mM NMN are shown. Bar graphs [(B) and (D)] represent means + SEM ($n = 7$). Asterisks indicate significant differences from the undifferentiated (0 hours) control (ANOVA; *$P < 0.05$; **$P < 0.01$). Representative images (C) show changes in nuclear NAD+ sensor fluorescence ratios during differentiation. Scale bars, 20 μm. Nuclear NAD+ levels (D) were, determined by the

sensor$_{(488/405\text{ nm})}$/control$_{(488/405\text{ nm})}$ fluorescence ratios using flow cytometry. (**E**) Western blots showing the rescue of PARP-1 enzymatic activity during early differentiation upon supplementation with 5 mM NMN. PAR levels indicate PARP-1 enzymatic activity. (**F** and **G**) Supplementation with exogenous NMN (5 mM) inhibits the differentiation of control 3T3-L1 and SVF cells (F), but not NMNAT-1– and PARP-1–depleted cells (G). The expression of adipocyte marker genes determined by RT-qPCR was used to assess the extent of differentiation. Each bar represents the mean + SEM ($n = 3$). Asterisks indicate significant differences versus the corresponding control (Student's *t* test; *$P < 0.05$, **$P < 0.01$, ***$P < 0.001$, ****$P < 0.0001$); ns, not significant (Student's *t* test; $P > 0.05$).

conclusion that NMNAT-2 induction depends on glucose metabolism (Fig. 5E). However, the increase in *Nmnat2* mRNA was not affected by glucose levels or inhibition of glycolysis (fig. S13A), and the inhibition of proteasome-mediated protein degradation prevented NMNAT-2 degradation upon glucose deprivation (fig. S13B), suggesting that the glucose-dependent modulation of NMNAT-2 levels occurs through posttranslational regulation.

Because PARP-1 PARylates C/EBPβ and inhibits its DNA binding (*14*), we hypothesized that a loss of NMNAT-2 induction upon glucose deprivation might alter C/EBPβ DNA binding. The expression of C/EBPβ was not affected by glucose metabolism, either at the mRNA or protein level (fig. S14, A and B). However, the binding of C/EBPβ to target gene promoters was dramatically reduced when glycolysis was inhibited during differentia-

tion (Fig. 5F), and adipogenesis was significantly reduced when glucose was deprived from the medium (fig. S15, A and B), suggesting that adipogenic transcription is regulated by glucose metabolism. The inhibitory effect of glucose deprivation on adipogenesis was abolished upon knockdown of *Nmnat1* and *Parp1* (fig. S15B), supporting the conclusion that metabolic regulation of adipogenic transcription is mediated by nuclear NAD⁺ synthesis and PARP-1.

A similar pathway for compartmentalized NAD⁺ biosynthesis exists in cancer cells

We further tested whether similar mechanisms play a key role in a completely different biological system. We focused on the SH-SY5Y human neuroblastoma cell line, which expresses a high

level of *NMNAT2* (fig. S16, A and B). Consistent with our observations in preadipocytes, knockdown of *NMNAT2* in SH-SY5Y cells significantly increased PARP-1 enzymatic activity (fig. S16C). In addition, *NMNAT2* knockdown inhibited the growth of the cells, suggesting that NMNAT-2 is important for cancer cell growth (fig. S16D). Moreover, glucose deprivation in SH-SY5Y cells also decreased the levels of NMNAT-2 protein and increased the enzymatic activity of PARP-1 (fig. S16, E and F). Collectively, these data suggest that compartmentalized NAD⁺ biosynthesis is not only important in adipogenesis, but can also play a key role in other biological processes, such as a cancer cell growth.

Discussion

Our studies have elucidated the pathway leading from enhanced glucose metabolism to the adipogenic
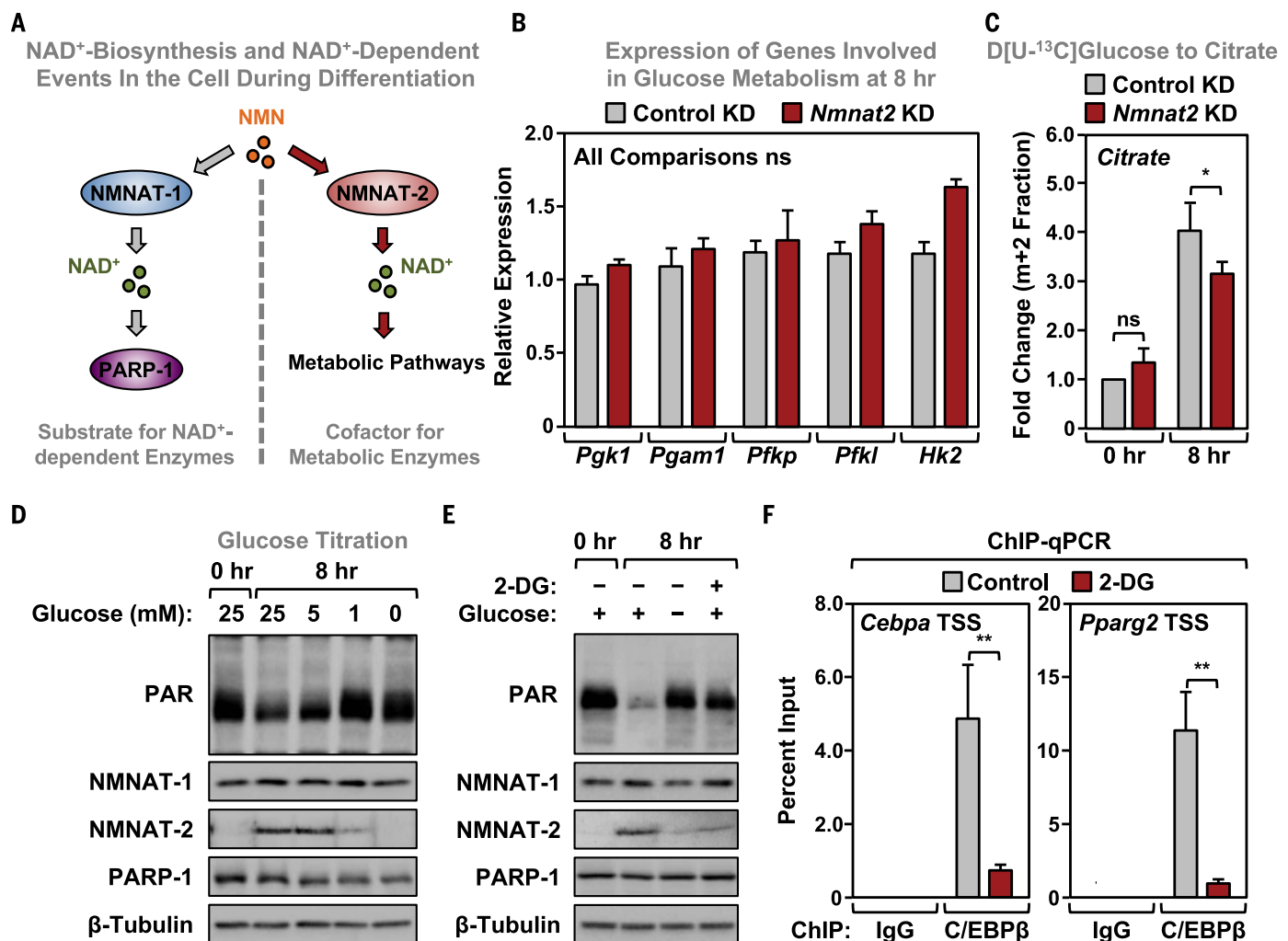
Fig. 5. NMNAT-2 induction is associated with enhanced glucose metabolism during the early phase of adipogenesis. (**A**) Schematic representation of the potential role of NMNAT-1 and NMNAT-2 during adipocyte differentiation. (**B**) *Nmnat2* knockdown does not affect the expression of genes involved in glucose metabolism after 8 hours of differentiation, as determined by RT-qPCR. None of the minor differences are significant (Student's *t* test; *P* > 0.05). (**C**) *Nmnat2* knockdown alters glucose flux during the differentiation of 3T3-L1 cells. Mass isotopomer analysis of citrate m+2 in cells with or without *Nmnat2* knockdown. Asterisks indicate

significant differences from the corresponding control (Student's *t* test; *P* < 0.05); ns, not significant (Student's *t* test; *P* > 0.05). (**D** and **E**) Expression of NMNAT-2 in 3T3-L1 cells differentiated in the presence of various extracellular glucose levels (D) or the glycolysis inhibitor 2-deoxyglucose (2-DG) (E) by Western blotting. (**F**) Regulation of C/EBPβ binding to target gene promoters in 3T3-L1 cells by ChIP-qPCR upon inhibition of glycolysis with 2-DG. The assays were done 8 hours postdifferentiation. Asterisks indicate significant differences from the corresponding control (Student's *t* test; **P** < 0.01). TSS, transcription start site. Throughout, bars represents means + SEM.
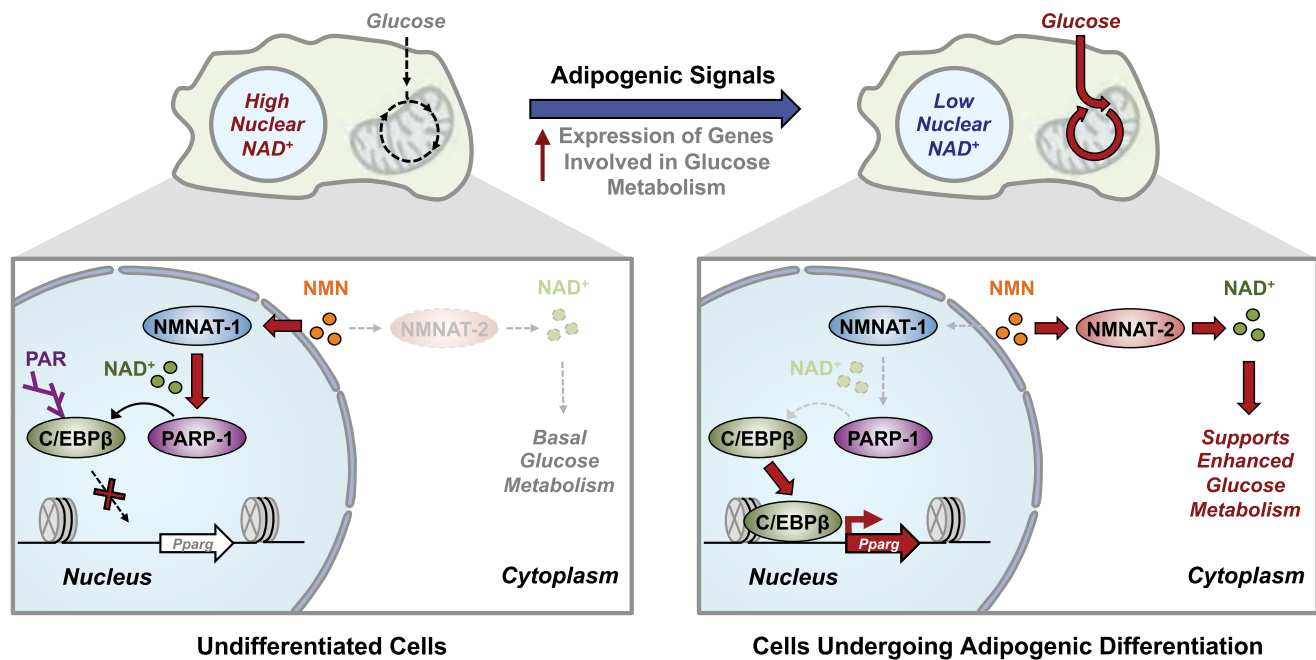
Fig. 6. Model for the coordination of transcription and glucose metabolism during adipocyte differentiation through compartmentalized NAD$^+$ biosynthesis. In undifferentiated 3T3-L1 cells, NMN is used mostly by NMNAT-1 to synthesize nuclear NAD$^+$, which supports PARP-1 activity. Active PARP-1 ADP-ribosylates the adipogenic transcription factor C/EBPβ, which inhibits its chromatin binding and transcriptional activities, preventing differentiation in the absence of an adipogenic signal. During differentiation, the expression of genes involved in glucose metabolism increases, leading to a rapid induction of glucose flux in 3T3-L1 cells. Concurrently, NMNAT-2 is rapidly induced to support the high local NAD$^+$ demands caused by enhanced glucose metabolism, thereby limiting NMN availability in the nucleus for NMNAT-1 to synthesize nuclear NAD$^+$. Reduced nuclear NAD$^+$ concentrations lead to reduced PARP-1 activity, allowing C/EBPβ to initiate the adipogenic transcription program. Competition for the NAD$^+$ precursor, NMN, between the nuclear and cytoplasmic NMNATs results in changes in nuclear NAD$^+$ levels, allowing cells to coordinate glucose metabolism and transcription.

gene expression program that drives the differentiation of adipocytes. Briefly, we have shown that compartmentalized NAD$^+$ biosynthesis is a crucial component of transcriptional regulation during adipocyte differentiation. Proper regulation of nuclear NAD$^+$ levels is achieved by the rapid induction of the cytosolic NAD$^+$-synthesizing enzyme, NMNAT-2, which consumes NMN in the cytoplasm, thereby limiting NMN availability in the nucleus. Reduced nuclear NMN levels lead to reduced nuclear NAD$^+$ synthesis, ultimately reducing PARP-1 enzymatic activity and C/EBPβ PARylation and enhancing C/EBPβ binding to target genes to drive the adipogenic transcription program (Fig. 6). Consistent with this model, decreasing nuclear NAD$^+$ synthesis by *Nmnat1* knockdown rapidly enhances differentiation, whereas increasing nuclear NAD$^+$ by NMN supplementation or *Nmnat2* knockdown inhibits adipogenesis. Compartmentalized NAD$^+$ biosynthesis is tightly linked to glucose metabolism, and increased glucose metabolism is required for the rapid induction of NMNAT-2, thus integrating cellular metabolism and the adipogenic transcription program. Collectively, our studies demonstrate that compartmentalized NAD$^+$ biosynthesis plays a key role in orchestrating intracellular metabolism and signal-regulated transcription. Such mechanisms likely play an important part in other biological systems that exhibit dramatic changes in nuclear PARylation as differentiation proceeds [e.g., embryonic stem cells (*24*)] or have a high glucose demand [e.g., cancer cells (*25*)].

Intracellular NAD$^+$ concentrations, compartmentalization, and biological outcomes

During differentiation, the free nuclear NAD$^+$ concentration, as measured by a nuclear NAD$^+$ sensor, drops from above PARP-1's K_m for NAD$^+$ (~100 μM) to below its K_m for NAD$^+$ (~40 μM) (Fig. 3C). This suggests that fluctuations in free nuclear NAD$^+$ have the ability to regulate the activity of PARP-1 and, perhaps, other nuclear NAD$^+$-dependent enzymes with suitable K_m values for NAD$^+$. The previously reported total intracellular NAD$^+$ concentration in cultured mammalian cells [~300 to 500 μM (*26*)] exceeds the estimated free NAD$^+$ concentration in the distinct subcellular compartments (Fig. 3C) (*20*). The disparity between total and free NAD$^+$ suggests that a portion of intracellular NAD$^+$ may be bound to protein, consistent with previous results (*26*). Therefore, cellular events that facilitate the release of protein-bound NAD$^+$ or, alternatively, promote the binding of NAD$^+$ to proteins could potentially alter the amount of free NAD$^+$ and consequently the enzymatic activity of NAD$^+$-consuming enzymes. Given that the free NAD$^+$ concentration is a key regulator of NAD$^+$-dependent enzymes, understanding the factors that regulate free versus bound NAD$^+$ could point to a previously unrecognized regulatory mechanism for NAD$^+$-dependent enzymes.

Our data show that nuclear NAD$^+$ biosynthesis is necessary for PARP-1–dependent regulatory events during the differentiation of preadipocytes. Such compartmentalization of metabolites, small molecules, and ions within the cell is not unprecedented. For example, cyclic adenosine monophosphate (cAMP) (*27*), Ca^{2+} (*28*), ATP (*29*), and acetyl–coenzyme A (CoA) (*30*) have also been reported to be compartmentalized and exhibit compartment-specific fluctuations in their concentrations. As with NAD$^+$, the precise mechanisms governing the compartmentalization and regulation of cAMP, Ca^{2+}, ATP, and acetyl-CoA are also unclear. In the case of nuclear versus cytoplasmic NAD$^+$, the diameter of the nuclear pore would not be expected to impose any physical barrier to the diffusion of NAD$^+$ between these two compartments (*31*). So how might compartmentalization occur?

One possibility is that cellular NAD$^+$ synthesis may be restricted to the site of consumption to support local demands, similar to cAMP, which is produced in distinct microdomains to increase local concentrations (*27*). This effect could be mediated by colocalization of metabolite producers and consumers, so that the consumers use the free metabolites as substrates before the metabolites can diffuse an appreciable distance away from their sources (*32*), perhaps through a

substrate-channeling mechanism (*33*). In this regard, NMNAT-1 binds to, colocalizes with, and regulates the enzymatic activity of PARP-1 and other chromatin-bound NAD$^+$-dependent enzymes at target gene promoters (*34*, *35*), which is consistent with a substrate-channeling mechanism.

Another possibility is that the nucleus and cytoplasm share a contiguous NAD$^+$ pool that can be altered independently and transiently in a temporal manner. Although the diffusion of small molecules should be extremely fast, reaching equilibrium rapidly when in free solution, diffusion rates can be inhibited considerably by molecular crowding inside the cell (*36*), which may allow cells to regulate metabolite pools in a compartment-specific manner. In this case, rapid and robust local changes in metabolite synthesis or consumption may cause local changes within a compartment that are not distributed across the entire pool. Indeed, we observed rapid induction of NMNAT-2 and glucose metabolism during differentiation (Fig. 3A and figs. S8, S9A, S9B, S11C, and S11D), suggesting that enhanced synthesis and consumption of NAD$^+$ in the cytoplasm under these conditions may restrict the diffusion of newly synthesized NAD$^+$. Further studies will be required to determine whether these or other mechanisms govern the compartmentalization and regulation of intracellular NAD$^+$.

Nuclear NAD$^+$ concentration and the activity of nuclear NAD$^+$-dependent enzymes

Although PARP-1 is considered to be the major NAD$^+$-consuming enzyme in the nucleus, other NAD$^+$-dependent enzymes, such as PARP-2, PARP-3, and SIRTs, are also present in the nucleus. Among these, SIRT1 has been reported to be a key regulator of various metabolic processes, with a catalytic activity that depends on intracellular NAD$^+$ concentrations (*7*). Thus, it is reasonable to speculate that fluctuations in nuclear NAD$^+$ levels may also regulate SIRT1 enzymatic activity. The reported K_m of SIRT1 for NAD$^+$ varies between 2.2 and ~300 μM, depending on the substrate and the study reporting the effect (*26*, *37*). If the K_m of SIRT1 for NAD$^+$ is below ~40 μM (*37*), then the changes that we observed in nuclear NAD$^+$ concentrations during the early phase of differentiation would not be sufficient to effect SIRT1 catalytic activity. In contrast, if the K_m of SIRT1 for NAD$^+$ is well above ~100 μM (*26*), then the changes that we observed in nuclear NAD$^+$ concentrations might possibly affect SIRT1 catalytic activity—but likely not nearly to the same extent as that of PARP-1, whose K_m is near the basal predifferentiation concentrations of NAD$^+$ in the preadipocytes (~100 μM was the highest nuclear NAD$^+$ concentration that we measured; Fig. 3C). Our results in 3T3-L1 cells favor the former possibility, because we observed a moderate effect of differentiation or *Nmnat1* knockdown on SIRT1 activity with acetylated H4K16 (histone H4 lysine 16) or acetylated p53 (fig. S3, C to F).

Although fluctuations in nuclear NAD$^+$ concentrations have little effect on SIRT1 enzymatic activity in 3T3-L1 cells, other regulatory mechanisms, such as allosteric regulatory interactions with NMNAT-1 at target gene promoters (*35*) or functional interactions with DBC-1 (*38*), may play an important role. These additional mechanisms, which could provide distinct approaches for the cell to regulate SIRT1 versus PARP-1, may be key to understanding the cell type– or tissue-specific regulation of NAD$^+$-dependent enzymes. *Nmnat1* knockdown significantly increased p53 acetylation levels in differentiated adipocytes (fig. S3, E and F), suggesting that SIRT1 activity is more sensitive to nuclear NAD$^+$ synthesis in mature adipocytes. This result supports previous reports that SIRT1 plays a critical role in adipocyte metabolism through PPAR$_\gamma$ regulation (*39*, *40*). Thus, NMNAT-1 and SIRT1 may play critical roles in fully differentiated adipocytes, but not the early stages of adipogenesis. In fact, the expression of *Sirt1* in preadipocytes is significantly lower than that of *Parp1* (fig. S3G) and increases during differentiation (*39*). These observations suggest that nuclear NAD$^+$ may regulate gene expression through distinct NAD$^+$-dependent enzymes in different biological processes, such as early adipogenesis versus mature adipocyte biology. Efforts to understand the biological importance of NMNATs have been largely limited to their function in neurodegeneration. However, given the role of NAD$^+$ as a universal metabolic cofactor and a substrate for enzymes that are known to regulate metabolic processes in a variety of tissues and cell types (*6*, *7*, *26*), we should expand our thinking about these NAD$^+$ biosynthetic enzymes. In particular, further exploration of their roles in compartment-specific NAD$^+$ synthesis and the regulation of metabolism in vivo is needed. The use of tissue-specific depletion of NMNATs, PARPs, and SIRTs will undoubtedly be required to resolve such questions in the future.

Materials and methods
Generation of Nmnat1 conditional knockout mice

Frozen *Nmnat1*$^{tm1a(EUCOMM)Wtsi}$ embryos on a C57BL/6N background were obtained from the International Mouse Phenotyping Consortium (IMPC; MGI ID 1913704) and were recovered at UT Southwestern's Transgenic Core Facility. All mice were housed and maintained at UT Southwestern's Animal Resource Center. The reporter cassette was removed by crossing *Nmnat1*$^{tm1a/tm1a}$ mice with FLP recombinase-expressing B6.129S4-*Gt(ROSA)26Sor*$^{tm2(FLP*)Sor}$/J mice (The Jackson Laboratory, stock no. 012930). After removing the reporter cassette, the resulting *Nmnat1*$^{loxP/+}$ mice were self-crossed to generate homozygous *Nmnat1*$^{loxP/loxP}$ progeny. To produce mice with a Tamoxifen-inducible conditional allele of *Nmnat1* (*Nmnat1*$^{loxP/loxP}$; *CAG-cre/ERT2*), *Nmnat1*$^{loxP/loxP}$ mice were crossed with transgenic mice containing a *CAG-cre/ERT2* cassette [B6.Cg-Tg(*CAG-cre/Esr1**)5Amc/J; The Jackson Laboratory, stock no. 004682]. All of the mouse genotypes were confirmed by short-range PCR, using PCR primers listed in the supplementary materials.

All of the studies with mice were performed according to IACUC guidelines under a protocol approved by UT Southwestern's Animal Use Committee.

Isolation of SVF cells from white adipose tissue

SVF cells were isolated as described previously (*41*). Briefly, 4- to 6-week-old male mice (2 mice per condition) were sacrificed and the inguinal white adipose tissue (WAT) was collected. The WAT was washed, pooled, minced, and digested for 2 hours at 37°C in 10 ml of digestion solution [100 mM HEPES pH 7.4, 120 mM NaCl, 50 mM KCl, 5 mM glucose, 1 mM CaCl$_2$, 1 mg/ml collagenase D (Roche, 11088858001), and 1.5% BSA]. The digested WAT tissue was filtered through a 100-μm cell strainer to remove undigested tissue, and 30 ml of SVF cell culture medium [10% FBS, 1% penicillin/streptomycin in DMEM/F12, GlutaMAX (Life Technologies, 10565-018)] was added to dilute the digestion buffer. The flow-through was centrifuged for 5 min at 600g to collect the SVF cells. The cell pellet was resuspended in 10 ml of SVF culture medium, and passed through a 40-μm cell strainer to remove clumps of cells and large adipocytes. The cells were collected again by centrifugation at 600g for 5 min, resuspended in SVF culture medium (5 ml per 2 mouse equivalents), and plated in a 6-cm-diameter collagen-coated culture dish until well attached.

Cell culture and differentiation

SVF cells (*16*, *17*) were grown in SVF culture medium until confluent and were then cultured for 2 more days under contact inhibition. The cells were then treated for 2 days with an adipogenic cocktail (MDI), including 0.5 mM IBMX (3-isobutyl-1-methylxanthine; Calbiochem, 410957), 1 μM dexamethasone (Sigma, D4902), and 5 μg/ml insulin (Sigma, I-5500). Subsequently, the cells were cultured in medium containing 5 μg/ml insulin for the indicated times before collection.

3T3-L1 cells (*15*) and NIH/3T3 cells were obtained from the American Type Cell Culture (ATCC, CL-173 and CRL-1658, respectively) and were mycoplasma-free. They were maintained in DMEM (Cellgro, 10-017-CM) supplemented with 10% fetal bovine serum (Atlanta Biologicals, S11550) and 1% penicillin/streptomycin. For the glucose titration experiments, the 3T3-L1 cells were grown in DMEM without glucose (Life Technologies, 11966-025). For the induction of adipogenesis, the 3T3-L1 cells were grown to confluence and then cultured for 2 more days under contact inhibition. The cells were then treated for 2 days with an MDI adipogenic cocktail containing 0.25 mM IBMX, 1 μM dexamethasone, and 10 μg/ml insulin. Subsequently, the cells were cultured in medium containing 10 μg/ml insulin for the indicated times before collection. For the induction of adipogenesis in NIH/3T3 cells, 1 μM Rosiglitazone (Sigma, R2408) was added to promote the differentiation process.

293T cells were obtained from the ATCC (CRL-3216) and were mycoplasma-free. They were maintained in DMEM (Cellgro, 10-017-CM) supplemented with 10% fetal bovine serum and 1% penicillin/streptomycin.

MCF-7 cells, kindly provided by Benita Katzenellenbogen (University of Illinois, Urbana-Champaign), were cultured in minimal essential medium (MEM; Sigma, M1018) supplemented with 5% calf serum (Sigma, C8056), 1% penicillin/streptomycin (Gibco, 15140122), and 25 μg/ml gentamicin (Gibco, 15710064).

MCF10A (CRL-10317), MDA-MB-231 (HTB-26), and SH-SY5Y (CRL-2266) cells were obtained from ATCC. MCF10A cells were cultured in mammary epithelial cell culture kit (Lonza, CC-2551B) and MDA-MB-231 cells were cultured in RPMI 1640 (Sigma, R8758) supplemented with 10% fetal bovine serum and 1% penicillin/streptomycin. SH-SY5Y cells were cultured in DMEM (Cellgro, 10-017-CM) supplemented with 20% fetal bovine serum and 1% penicillin/streptomycin.

Cell treatments

3T3-L1 or SVF were exposed to various treatments and culture conditions for the experiments described herein. For treatment with NMN (1 mM or 5 mM; Sigma, N3501), MG-132 (10 μM, Sigma, M7449), or 2-deoxy-D-glucose (5 mM; Sigma, D8375), the cells were grown until confluent and then pretreated with either compound for 2 hours prior to the addition of the MDI cocktail. The cells were then differentiated in medium with MDI in the presence of NMN or 2-deoxy-D-glucose for the indicated times before collection. For differentiation longer than 2 days, the compounds were added to the medium with MDI for 2 days, then removed when changing culture medium. For SIRT1 inhibition, the cells were treated with 10 μM Sirtinol (Calbiochem, 566320) for 48 hours before collection. For the Dox-inducible system, we treated the cells with 1 μg/ml (for NAD$^+$ sensors and Dox-inducible knockdown) or 250 ng/ml (for NMNAT-2 overexpression) Dox for 48 hours. For NAMPT inhibition, we treated the cells with 50 nM FK866 (Sigma, F8557) for 48 hours. For Tamoxifen-inducible, Cre-mediated *Nmnat1* deletion, *Nmnat1$^{loxP/loxP}$; CAG-CreERT2* SVF cells were cultured until confluent and were then treated with 1 μM 4-hydroxytamoxifen (4-OHT; Sigma, H7904) for 2 days before the induction of adipogenesis, as described above.

Antibodies

The custom rabbit polyclonal antiserum against PARP-1 used for Western blotting and ChIP assays was generated by using a purified recombinant antigen comprising the amino-terminal half of PARP-1 (*42*) (now available from Active Motif; cat. no. 39559). The custom rabbit polyclonal antiserum against NMNAT-1 was raised against purified recombinant human and mouse NMNAT-1 (Pocono Rabbit Farm and Laboratory). The custom recombinant antibody-like anti-poly-ADP-ribose binding reagent (anti-PAR) was generated and purified in-house (now available from EMD Millipore, MABE1031). The other antibodies used were as follows: C/EBPβ (Santa Cruz, sc-150X), NMNAT-2 (Abcam, ab56980), β-Tubulin (Abcam, ab6046), SIRT1 [custom rabbit polyclonal antiserum raised against mouse SIRT1 (*35*)], acetyl-p53 K379 (Cell signaling, #2570), p53 (Cell signaling,

#2524), H4K16Ac (Millipore, 07-329), Histone H4 (Millipore, 07-108), rabbit IgG (Invitrogen, 10500C), goat anti-rabbit HRP-conjugated IgG (Pierce, 31460), and goat anti-mouse HRP-conjugated IgG (Pierce, 31430).

Molecular cloning to generate expression and knockdown vectors

shRNAs targeting Nmnat1, Parp1, and NMNAT2

shRNA constructs targeting mouse *Nmnat1* mRNA (TRCN0000111435, TRCN0000335596) and control shRNA (SHC002) were purchased from Sigma. We generated an shRNA construct targeting mouse *Parp1* mRNA by cloning a double-stranded oligonucleotide (5′-GGGCAAGCACAGTGTCAAA-3′) into the pLKO.1 vector (SHC001), which confers puromycin resistance. Dox-inducible shRNA sequences targeting human *NMNAT2* mRNA were purchased from Dharmacon (V3THS400729, V3THS400730, V3THS_400733) and were cloned individually, along with a corresponding control shRNA targeting luciferase, into the pTRIPZ vector using a double-stranded oligonucleotide (5′-AGATATGGCTGAA-TACAAATC-3′).

RNAi-resistant Nmnat1 expression constructs

cDNA was prepared by extracting total RNA from 3T3-L1 cells using Trizol (Invitrogen, 15596026), followed by reverse transcription using superscript III reverse transcriptase (Invitrogen, 18080051) and an oligo(dT) primer according to manufacturer's instructions. *Nmnat1* cDNA was then amplified from the cDNA library and cloned into the pBabe-neo (Addgene, 1767) retroviral expression vector using the primers listed in the supplementary materials. cDNAs for an RNAi-resistant mutant and a catalytically inactive mutant (W170A) were generated by site-directed mutagenesis using Pfu Turbo DNA polymerase (Agilent, 600250) with the primers listed in the supplementary materials.

Quantitative cpVenus-based NAD$^+$ sensor constructs

Expression vectors for cpVenus-based nuclear and cytoplasmic NAD$^+$ sensors and their corresponding cpVenus-only controls (*20*) were kindly provided by M. Cohen and R. Goodman. DNA coding for the sensors or controls was amplified from the expression vectors provided using the primers listed in the supplementary materials and then cloned into the pINDUCER20 lentiviral Dox-inducible expression vector (Addgene, plasmid no. 44012) (*43*) using Gibson assembly (NEB, E2621).

Dox-inducible Nmnat2 expression constructs

cDNA was prepared as described above. *Nmnat2* cDNA was then amplified from the cDNA library and cloned into pINDUCER20 lentiviral Dox-inducible expression vector using the primers listed in the supplementary materials. A catalytically inactive *Nmnat2* mutant (H24D) was generated by site-directed mutagenesis using Pfu

Turbo DNA polymerase using the primers listed in the supplementary materials.

Generation of cell lines with stable knockdown or ectopic expression

Cells were transduced with either lentiviruses or retroviruses for stable knockdown or ectopic expression. We generated lentiviruses by transfection of the pLKO.1 constructs described above, together with: (i) an expression vector for the VSV-G envelope protein (pCMV-VSV-G, Addgene plasmid no. 8454), (ii) an expression vector for GAG-Pol-Rev (psPAX2, Addgene plasmid no. 12260), and (iii) a vector to aid with translation initiation (pAdVAntage, Promega) into 293T cells using GeneJuice transfection reagent (Novagen, 70967) according to the manufacturer's protocol. The resulting viruses were collected in the culture medium, concentrated by using a Lenti-X concentrator (Clontech, 631231), and used to infect cells.

Retroviruses were generated by transfection of the pMSCV constructs described above, together with an expression vector for the VSV-G envelope protein (pCMV-VSV-G), into Phoenix Ampho cells using GeneJuice transfection reagent (Novagen, 70967) according to the manufacturer's protocol. The resulting viruses were used to infect.

Stably transduced cells were selected with puromycin (Sigma, P9620; 2 μg/ml) or G418 sulfate (Sigma, A1720; 1 mg/ml).

Knockdown of Nmnat2 using siRNAs

Commercially available siRNA oligos targeting *Nmnat2* (Sigma, SASI_Mm01_00083355, SASI_Mm01_00083356, and SASI_Mm01_00083357) were transfected at a final concentration of 20 nM using Lipofectamine RNAiMAX reagent (Invitrogen, 13778150) according to the manufacturer's instructions. All experiments were performed 48 hours after siRNA transfection.

Preparation of cell lysates and Western blotting

3T3-L1 and SVF cells were cultured and differentiated as describe above. The cells were then washed twice with ice-cold PBS and lysed with Lysis Buffer (20 mM Tris-HCl pH 7.5, 150 mM NaCl, 1 mM EDTA, 1 mM EGTA, 1% NP-40, 1% sodium deoxycholate, 0.1% SDS) containing 1 mM DTT, 250 nM ADP-HPD (Sigma, A0627; a PARG inhibitor to prevent PAR chain cleavage during extraction), 10 μM PJ34 (a PARP inhibitor to prevent PAR synthesis during extraction), and 1x complete protease inhibitor cocktail (Roche, 11697498001). For measuring SIRT1 activity, 10 mM sodium butyrate (a class I/II HDAC inhibitor) and 10 μM Sirtinol (a sirtuin inhibitor) were added to the lysate to prevent deacetylation during extraction. For the chromatin fractions, lysed cells were sonicated in Lysis Buffer to solubilize the chromatin. For the nuclear and cytoplasmic fractions, the cells were first resuspended in Isotonic Buffer (10 mM Tris-HCl pH 7.5, 2 mM MgCl$_2$, 3 mM CaCl$_2$, 0.3 M sucrose, 1 mM DTT, and 1x complete protease inhibitor cocktail), incubated on ice for 15 min, and lysed by the addition of 0.6% IGEPAL

CA-630 detergent with gentle vortexing. The nuclei from the lysed cells were pelleted by centrifugation, and the supernatant was collected as the cytoplasmic fraction. The pelleted nuclei were resuspended in Nuclear Extraction Buffer (50 mM Tris-HCl pH 7.4, 500 mM NaCl, 1 mM EDTA, 1% IGEPAL CA-630, 1 mM DTT, and 1x complete protease inhibitor cocktail) to produce the nuclear lysate. All lysates were incubated on ice for 30 min for extraction and then centrifuged to clarify. The supernatants were collected, run on a 6% polyacrylamide-SDS gel (for PARP-1 and PAR analyses) or a 10% polyacrylamide-SDS gel (for NMNAT-1, C/EBPβ, NMNAT-2, β-tubulin), and transferred to a nitrocellulose membrane. The membranes were blocked with 5% nonfat milk in TBST and incubated with the primary antibodies described above in 1% nonfat milk in TBST, followed by anti-rabbit HRP-conjugated IgG (1:5000) or anti-mouse HRP-conjugated IgG (1:3000). Western blot signals were detected using an ECL detection reagent (Thermo Fisher, 34077, 34095).

GTEx tissue expression analyses

The expression profiles of *NMNAT1* and *NMNAT2* in different human tissues was determined based on RPKM values using GTEx (*44*) (www.gtexportal.org/home/) with dbGaP Study Accession phs000424.v6.p1 (www.ncbi.nlm.nih.gov/projects/gap/cgi-bin/study.cgi?study_id=phs000424.v6.p1).

RNA isolation and RT-qPCR

3T3-L1 cells or SVF cells were seeded at ~2×10^5 cells per well in 6-well plates and treated as described above. For tissue RNA isolations, 6- to 8-week-old C57BL/6 male mice were used. The cells and tissues were collected and total RNA was isolated using Trizol Reagent (Invitrogen) according to the manufacturer's protocols. Total RNA was reverse transcribed using oligo (dT) primers and MMLV reverse transcriptase (Promega) to generate cDNA. The cDNA samples were subjected to qPCR using gene-specific primers, as described below. For the reverse transcription quantitative real-time PCR (RT-qPCR) analyses, "relative expression" was determined in comparison to a value from the first biological replicate of the control sample. Target gene expression was normalized to the expression of *Tbp* mRNA (mouse) or *RPL19* mRNA (human). The normalized value from the first biological replicate of the control sample was set to 1 and all the rest of the values, including the values from other biological replicate of controls, were plotted against it. All experiments were performed a minimum of three times with independent biological replicates to ensure reproducibility and a statistical significance of at least $P < 0.05$. Statistical differences between control and experimental samples were determined using the Student's *t* test. All experimental groups that were compared had similar variance as determined by the standard deviation of the biological replicates within each group.

ChIP-qPCR

3T3-L1 cells were cultured, differentiated, and treated as described above in 15-cm-diameter plates. ChIP was performed as described previously (*45*, *46*), with slight modifications. Briefly, the cells were cross-linked with 1% formaldehyde in PBS for 10 min at 37°C and quenched in 125 mM glycine in PBS for 5 min at 4°C. Cross-linked cells were then collected by centrifugation and lysed in Farnham Lysis Buffer (5 mM PIPES pH 8.0, 85 mM KCl, 0.5% NP-40, 1 mM DTT, and 1x complete protease inhibitor cocktail). A crude nuclear pellet was collected by centrifugation, resuspended in Sonication Buffer (50 mM Tris-HCl pH 7.9, 1% SDS, 10 mM EDTA, 1 mM DTT, and 1x complete protease inhibitor cocktail), and sonicated to generate chromatin fragments of ~300 bp in length. The soluble chromatin was clarified by centrifugation, diluted 1:10 with Dilution Buffer (20 mM Tris-HCl pH 7.9, 0.5% Triton X-100, 2 mM EDTA, 150 mM NaCl, 1 mM DTT, and 1x complete protease inhibitor cocktail) and pre-cleared with protein A agarose beads.

The pre-cleared samples were used in immunoprecipitation reactions with antibodies against C/EBPβ or with rabbit IgG (as a control) with incubation overnight at 4°C. The samples were washed with Low Salt Wash Buffer (20 mM Tris-HCl pH 7.9, 2 mM EDTA, 125 mM NaCl, 0.05% SDS, 1% Triton X-100, 1 µM aprotinin, and 1 µM leupeptin), High Salt Wash Buffer (20 mM Tris-HCl pH 7.9, 2 mM EDTA, 500 mM NaCl, 0.05% SDS, 1% Triton X-100, 1 µM aprotinin, and 1 µM leupeptin), LiCl Wash Buffer (10 mM Tris-HCl, pH 7.9, 1 mM EDTA, 250 mM LiCl, 1% NP-40, 1% sodium deoxycholate, 1 µM aprotinin, and 1 µM leupeptin), and 1x Tris-EDTA (TE). The immunoprecipitated genomic DNA was eluted in Elution Buffer (100 mM NaHCO3, 1% SDS), digested with proteinase K and RNase H to remove protein and RNA, respectively, and then extracted with phenol:chloroform:isoamyl alcohol. The ChIPed genomic DNA was subjected to qPCR using gene-specific primers, as described below. The immunoprecipitation of genomic DNA was normalized to the input. All experiments were performed a minimum of three times with independent biological replicates to ensure reproducibility and a statistical significance of at least $P < 0.05$. Statistical differences between control and experimental samples were determined using the Student's *t* test. All experimental groups that were compared had similar variance as determined by the standard deviation of the biological replicates within each group.

qPCR

qPCR was performed as described previously (*47*). Briefly, cDNA or ChIPed DNA samples were mixed with 1x SYBR Green PCR master mix and primers (forward and reverse, 250 nM), and were then subjected to 45 cycles of amplification (95°C for 10 s, 60°C for 10 s, 72°C for 1 s) following an initial 5 min incubation at 95°C using a Roche LightCycler 480 384-well detection system. Melting curve analyses were performed to ensure that only the targeted amplicon was amplified. All qPCR-based experiments were performed a minimum of three times with independent biological replicates to ensure reproducibility and a statistical significance of at least $P < 0.05$. Statistical differ-ences between control and experimental samples were determined using the Student's *t* test. All experimental groups that were compared had similar variance as determined by the standard deviation of the biological replicates within each group. The sequences of the primers are listed in the supplementary materials.

RNA-seq
Generation of RNA-seq libraries

Two biological replicates of control, *Nmnat1*, and *Parp1* knockdown 3T3-L1 cells were differentiated as described above. Total RNA was isolated using the RNeasy kit (Qiagen) according to the manufacturer's instructions. The total RNA was then enriched for polyA+ RNA using Dynabeads Oligo(dT)25 (Invitrogen). The polyA+ RNA was then used to generate strand-specific RNA-seq libraries as described previously (*48*). The RNA-seq libraries were subjected to QC analyses (i.e., number of PCR cycles required to amplify each library, the final library yield, and the size distribution of final library DNA fragments) and sequenced using an Illumina HiSeq 2000.

Analysis of RNA-seq data

The raw data were subjected to QC analyses using the FastQC tool (*49*). The reads were then mapped to mouse genome (mm10) using the spliced reader aligner TopHat version 2.0.13 (*50*). Transcriptome assembly was performed using cufflinks v.2.2.1 (*51*) with default parameters. The transcripts were merged into two distinct, nonoverlapping sets using cuffmerge, followed by cuffdiff to call the differentially regulated transcripts. The significantly ($P < 0.05$) regulated genes upon *Nmnat1* or *Parp1* knockdown compared to control knockdown at the indicated time points were used to find the commonly regulated gene set. Similar analyses were performed with published RNA-seq data sets (GSE57415, GSE29899).

Linking transcription factors to gene regulation using PCHi-C data

In order to determine the transcription factors that bind upstream of the NMNAT-1 and PARP-1 commonly regulated genes, we queried publicly available ChIP-seq data sets for C/EBPβ, STAT5A, RXRα, C/EBPδ, and GR (NCBI GEO accession number GSE27826) (*19*) and the called peaks from these data sets were lifted over to mm10. To determine which transcription factors interact with the promoters of PARP-1 and NMNAT-1 co-regulated genes, raw sequence reads from published PCHi-C data (GSE95533) (*18*) were processed using the HiCUP pipeline (*52*), which maps the positions of di-tags against the mouse genome (mm10), filters out experimental artifacts (e.g., circularized reads and re-ligation products), and removes all duplicate reads. Hicpipe (*53*), version 0.9 was used to correct the PCHi-C contact maps using the restriction enzyme site HindIII and the mapped paired reads. A custom script (available from W.L.K. upon request) was used to define all the interactions between the promoters and the transcription factor binding sites. The genomic loci interacting with the promoters of genes

co-regulated by *Nmnat1* and *Parp1* knockdown were compared to the individual transcription factor ChIP-seq peaks to identify the promoter-transcription factor binding site interactions. The number of NMNAT-1 and PARP-1 regulated genes containing significant ChIP-seq peaks of the specified transcription factors at their interacting genomic loci were divided by the total number of NMNAT-1/PARP-1 co-regulated genes to determine the percent of co-regulated gene promoters interacting with each transcription factor.

To determine the expression levels of the genes whose promoters interact with C/EBPβ binding sites, we first identified C/EBPβ binding sites using ChIP-seq data (GSE27826) and then determined all the promoters interacting with these binding sites using PCHi-C (GSE95533). Among these gene promoters, we took only the genes expressed in 3T3-L1 cells (FPKM > 1) during differentiation. The expression level of these genes (determined by RNA-seq) in control, *Nmnat1* and *Parp1* knockdown 3T3-L1 cells at day 2 or 4 was compared to the control knockdown at day 0 to calculate the fold change for each gene. Up-regulated genes were defined as fold change greater than 1. All custom scripts are available by request from W.L.K.

Genomic data sets

The new RNA-seq generated for this study can be accessed from the NCBI's Gene Expression Omnibus (GEO) repository (www.ncbi.nlm.nih.gov/geo/) using the accession number GSE96764.

Intracellular lipid staining
BODIPY staining

3T3-L1 cells were seeded on sterile cover slips in 24-well plates and differentiated as described above. The cells were rinsed twice with 1x PBS and fixed with 4% paraformaldehyde. The fixed cells were washed twice with 1x PBS and stained with 1 μg/ml of BODIPY 493/503 (Life Technologies, D3922) for 10 min. The cells were then washed three times with 1x PBS and counter-stained with 1 μM TO-PRO-3 (Life Technologies, T3605) for 2 min. The cover slips were then mounted onto glass slides with VECTASHIELD Mounting Medium (Vector Laboratories, H-1000). Confocal images were acquired using a Leica SP2 confocal microscope.

Oil Red O staining

3T3-L1 cells were cultured in 6-well plates and differentiated as described above. After 8 days of differentiation, the cells were rinsed twice with 1x PBS and fixed with 4% paraformaldehyde. The fixed cells were washed with water and incubated in 60% isopropanol for 5 min. After incubation, the isopropanol was removed and replaced with 0.3% Oil-red-O working solution for 5 min. The Oil Red O working solution was prepared by diluting a stock solution (0.5% in isopropanol; Sigma, O1391) with water (3:2).

Measurement of total intracellular NAD⁺ levels

3T3-L1 cells were cultured and differentiated as described above. For NAD⁺ measurements, the cells were harvested with 0.5 M perchloric acid and neutralized with and equal volume of 0.55 M of K_2CO_3. The samples were then centrifuged and the supernatants were collected for metabolite measurement. Total intracellular NAD⁺ or NADH levels were measured using a NAD⁺/NADH colorimetric assay kit (Cyclex, CY-1253) following the manufacturer's instructions. For the NAD⁺ measurement, "relative level" was determined in comparison to a value from the first biological replicate of the control sample. A value from the first biological replicate of the control sample was set to 1 and all the rest of the values were plotted relative to that.

Determination of nuclear and cytoplasmic NAD⁺ levels using cpVenus-based sensors

3T3-L1 cells expressing nuclear or cytoplasmic NAD⁺ sensors and their corresponding cpVenus-only controls were used to measure changes in subcellular NAD⁺ levels. The cells were treated with 1 μg/ml Dox to induce expression of the sensors for 48 hours prior to the experiment. The NAD⁺ sensor experiments were performed as described previously (20), with details provided below.

Purification of sensor proteins

Expression vectors for the sensors and their corresponding cpVenus-only controls (described above) were transfected into 293T cells using lipofectamine 3000 (Thermo Fisher, L3000015) following the manufacturer's protocol. After 48 hours, the cells were washed twice with ice-cold PBS and collected via centrifugation. Whole cell extracts were prepared from the cells expressing the cytoplasmic sensor or the corresponding cytoplasmic control by resuspending the cells in Lysis Buffer [50 mM Tris-HCl pH 7.4, 150 mM NaCl, 1 mM EDTA, 0.5% IGEPAL CA-630, 1 mM DTT, and 1x complete protease inhibitor cocktail (Roche)], incubating them for 30 min at 4°C, and then clarifying the lysate by centrifugation. Extracts were prepared from the cells expressing the nuclear sensor or the corresponding nuclear control, by resuspending the cells in Isotonic Buffer (10 mM Tris-HCl pH 7.5, 2 mM $MgCl_2$, 3 mM $CaCl_2$, 0.3 M sucrose, 1 mM DTT, and 1x complete protease inhibitor cocktail), incubating them on ice for 15 min, and lysing them by the addition of 0.6% IGEPAL CA-630 detergent with gentle vortexing. The nuclei from the lysed cells were collected by centrifugation, resuspended in Nuclear Extraction buffer (50 mM Tris-HCl pH 7.4, 150 mM NaCl, 1 mM EDTA, 1% IGEPAL CA-630, 1 mM DTT, and 1x complete protease inhibitor cocktail), and incubated for 30 min at 4°C. The resulting nuclear extract was clarified by centrifugation. Both the whole cell and nuclear extracts were incubated with anti-FLAG M2 affinity gel (Sigma, A2220) at 4°C for 4 hours to allow binding of the FLAG-tagged sensors and controls. The resin was washed five times in either the Lysis Buffer or the Nuclear Extraction Buffer, respectively, for 10 min at 4°C with constant mixing. The proteins were eluted with 500 μg/ml of 3x FLAG peptide (Sigma, F4799)

made in wash buffer. The eluates were dialyzed in Dialysis Buffer (100 mM Tris-HCl pH 7.4, 150 mM NaCl, 1 mM EDTA, 0.5 mM DTT, 100 μM PMSF, and 20% glycerol). The concentrations of the protein solutions were measured using Bradford assays. The purity of the sensor and control proteins was confirmed by SDS-PAGE with subsequent silver staining using a Pierce silver staining kit (Thermo Fisher, 24600) following the manufacturer's protocol.

Measurement of in vitro fluorescence changes using spectroscopy

Purified sensor and control proteins (250 nM) were incubated with the indicated amount of NAD⁺ in total reaction volume of 75 μl. The samples were incubated at RT for 15 min and the fluorescence was measured using a Spark 20M plate reader (Tecan). Excitation and emission spectra were 488 nm and 530 nm, respectively, with slit widths of 5 nm band pass for the excitation and 10 nm band pass for the emission. A standard curve was generated using the ratio of fluorescence values (sensor fluorescence/cpVenus fluorescence), which were fitted to a sigmoidal regression model using GraphPad Prism 7.

Imaging

3T3-L1 cells were seeded on chambered cover slips (Thermo Fisher, 155411) and cultured in FluoroBrite media (Thermo Fisher, A1896701) supplemented with 10% FBS (TET tested; Atlanta Biologicals, S103050) and 1% penicillin/streptomycin. Images were acquired using an inverted Zeiss LSM 780 confocal microscope affixed with a 37°C, 5% CO2 incubator. To measure NAD⁺-dependent fluorescence changes, both the sensor and its corresponding cpVenus-only control were imaged with excitation at 488 nm and emission at 525 nm. The signal levels from the sensors and the controls were measured with excitation at 405 nm and emission at 525 nm.

Image analysis

We used Image J software to subtract background, set thresholds, select the regions of interest (ROIs), and quantify fluorescence intensity. Ratiometric analyses (488/405 nm) of the sensor versus control were used to normalize sensor expression levels and to analyze the changes in subcellular NAD⁺ levels. To generate a pixel-by-pixel ratiometric images, we used a custom MATLAB program (available by request from W.L.K.). Average ratiometric values for the undifferentiated 3T3-L1 cells were defined as 1, and the rest of the data were normalized accordingly.

Flow cytometry

3T3-L1 cells were cultured and differentiated as described above. For flow cytometry analysis, the cells were trypsinized and triturated with FluoroBrite media containing 10% FBS and 1% penicillin/streptomycin. The data were collected on a BD Biosciences LSR II flow cytometer. The cells were gated using forward scatter (FSC) and side scatter (SSC) for the live cells and then further gated on both SSC and FSC width to ensure that individual cells were analyzed. FITC (excitation

488 nm, emission 530/30 nm) and BV510 (excitation 405 nm, emission 525/50 nm) were used for the sensor and control fluorescence. For the nuclear control, cytoplasmic sensor, and cytoplasmic control, we analyzed 1×10^4 cells. For the nuclear sensor, we analyzed 5×10^4 cells due to lower expression levels of the sensor. 3T3-L1 cells without fluorescent protein were used as a negative control to set a threshold for the analysis. The data were analyzed with FlowJo software and sensor/control ratiometric analyses were performed using a derived function on the software. Cells with high levels of sensor or control signals (about 5×10^3 cells per condition in each biological replicates) were subjected to ratiometric analysis (488/405 nm) to obtain the values for each cell. Geometric mean fluorescence intensity of the ratio was determined for each condition, and the values for sensor were divided by the values for the corresponding cpVenus-only control to account for any pH effects [sensor (488/405)/cpVenus (488/405)] (20). Changes in subcellular NAD$^+$ levels were analyzed by normalizing the values relative to undifferentiated or vehicle treated 3T3-L1 cells. All experiments were performed a minimum of three times with independent biological replicates to ensure reproducibility and a statistical significance of at least $P < 0.05$. Statistical differences between control and experimental samples were determined using ANOVA or Student's *t* test. All experimental groups that were compared had similar variance as determined by the standard deviation of the biological replicates within each group.

Permeabilization of cells to NAD$^+$

3T3-L1 cells expressing a sensor and the corresponding cpVenus-only control were cultured as described above. To generate NAD$^+$ dose-response curves for the sensors, the cells were trypsinized and suspended with FluoroBrite media containing 10% FBS and 1% penicillin/streptomycin. The cells were then permeabilized with 0.001% digitonin while exposed to the indicated amounts of NAD$^+$ with incubation at RT for 15 min. The samples were subjected to flow cytometry and analyzed as described above. All of the values were plotted relative to the values obtained using 10 μM NAD$^+$ from 8 replicates. For image analysis, the cells were cultured in chambered cover slips as described above. After acquiring images for untreated conditions, 0.001% digitonin and the indicated amount of NAD$^+$ were added to the media, equilibrated for 15 min to obtain NAD$^+$-dependent changes in signal. The images were analyzed as described above.

Quantification of intracellular NAD$^+$ levels

To determine the intracellular NAD$^+$ levels, the standard curve generated from the NAD$^+$ permeabilization assays described above were fitted to a sigmoidal regression model using GraphPad Prism 7 $\left\{ y = \min + \left[\frac{\max - \min}{1 + 10^{(\log IC50 - \chi) \, x \, \text{Hillslope}}} \right] \right\}$. The ratiometric values relative to 10 μM NAD$^+$ were entered into the equation as a y value to calculate the intracellular (nuclear or cytoplasmic) NAD$^+$ levels. An average of 32 replicates from 11 in-

dependent experiments were interpolated to obtain values for x. To measure the changes in NAD$^+$ levels under different experimental conditions, the fluorescence ratio was measured using flow cytometry, as described above, and normalized to the control conditions (e.g., undifferentiated 3T3-L1). The NAD$^+$ concentrations were then determined from the standard curve using ratiometric values in comparison to the values from undifferentiated 3T3-L1. For the estimation of cytoplasmic NAD$^+$ levels at 8 hours postdifferentiation upon *Nmnat2* knockdown, the fluorescence ratio was measured using flow cytometry as described above, and the relative NAD$^+$ level compared to the control knockdown was determined. The estimated NAD$^+$ concentration was calculated based on the assumption that the cytoplasmic NAD$^+$ concentration at 8 hours postdifferentiation in control knockdown cells were similar to the measured cytoplasmic NAD$^+$ levels in 3T3-L1 cells at 8 hours of differentiation.

Analysis of metabolic flux

3T3-L1 cells were grown to confluence, and then grown for another 2 days under contact inhibition. Induction of adipogenesis was achieved as described above until indicated time points. To quantify different mass isotopomers of intracellular citrate by GC/MS (54), the cells were washed with PBS and incubated in medium containing an isotopically enriched nutrient (i.e., D[U-^{13}C] glucose and unlabeled glutamine for measuring glucose flux) for 1 min or 5 min. Labeled cells were then rinsed with ice-cold 0.9% saline and lysed with three freeze-thaw cycles in cold 50% methanol/50% water. The lysates were centrifuged to remove precipitated proteins and a standard (50 nmol of sodium 2-oxobutyrate) was added. The samples were then evaporated and derivatized using tertbutyldimethylsilyl (TBDMS, Sigma) (55). One microliter of the derivatized sample was injected into an Agilent 6970 gas chromatograph equipped with a fused silica capillary GC column and networked to an Agilent 5973 mass selective detector. Retention times of citrate were validated using pure standards. The abundance of the citrate ions was monitored at m/z 459, pyruvate at m/z 174-177, and lactate at m/z 261-264. The measured distribution of mass isotopomers was corrected for the natural abundance of ^{13}C. M+2 indicates the percent enrichment of citrate, two carbons of which were ^{13}C-labeled, providing a measure of glucose flux through the TCA cycle.

Analysis of lactate secretion

3T3-L1 cells were cultured in 6-well plates as described above. siRNAs were transfected 48 hours prior to the experiments and the cells were differentiated as described above for the indicated times. The media was collected and the assay was performed using a glycolysis cell-based assay kit (Cayman Chemical, 600450) following the manufacturer's instructions.

NMNAT2 expression in cancer cells

The expression profiles of *NMNAT2* in different cancer cells was determined based on TPM

values from the Cancer Cell Line Encyclopedia (CCLE). CCLE data was downloaded from the web-based omics platform OASIS (http://www.oasis-genomics.org/).

Cell proliferation assays

SH-SY5Y cells expressing Dox-inducible shRNAs targeting luciferase or *NMNAT2* were plated at a density of 1×10^5 cells per well in 6-well plates and were induced using 1 μg/ml doxycycline added to the medium (Day 0). After 24 hours, the medium was removed and replaced with fresh medium containing 1 μg/ml of doxycycline. The cells were grown until the indicated time points, with replacement of the medium every 48 hours. The cells were then fixed with 10% formaldehyde and stained with 0.1% crystal violet in 75 mM phosphoric acid. After washing with a copious amount of water, the crystal violet was extracted from the cells using 10% acetic acid and measured as absorbance at 562 nm.

REFERENCES AND NOTES

1. C. Lu, C. B. Thompson, Metabolic regulation of epigenetics. *Cell Metab.* **16**, 9–17 (2012). doi: 10.1016/j.cmet.2012.06.001; pmid: 22768835
2. A. E. Boukouris, S. D. Zervopoulos, E. D. Michelakis, Metabolic enzymes moonlighting in the nucleus: Metabolic regulation of gene transcription. *Trends Biochem. Sci.* **41**, 712–730 (2016). doi: 10.1016/j.tibs.2016.05.013; pmid: 27345518
3. J. A. van der Knaap, C. P. Verrijzer, Undercover: Gene control by metabolites and metabolic enzymes. *Genes Dev.* **30**, 2345–2369 (2016). doi: 10.1101/gad.289140.116; pmid: 27881599
4. A. Chiarugi, C. Dölle, R. Felici, M. Ziegler, The NAD metabolome— a key determinant of cancer cell biology. *Nat. Rev. Cancer* **12**, 741–752 (2012). doi: 10.1038/nrc3340; pmid: 23018234
5. B. A. Gibson, W. L. Kraus, New insights into the molecular and cellular functions of poly(ADP-ribose) and PARPs. *Nat. Rev. Mol. Cell Biol.* **13**, 411–424 (2012). doi: 10.1038/nrm3376; pmid: 22713970
6. K. W. Ryu, D. S. Kim, W. L. Kraus, New facets in the regulation of gene expression by ADP-ribosylation and poly(ADP-ribose) polymerases. *Chem. Rev.* **115**, 2453–2481 (2015). doi: 10.1021/cr5004248; pmid: 25575290
7. R. H. Houtkooper, E. Pirinen, J. Auwerx, Sirtuins as regulators of metabolism and healthspan. *Nat. Rev. Mol. Cell Biol.* **13**, 225–238 (2012). doi: 10.1038/nrm3293; pmid: 22395773
8. A. G. Cristancho, M. A. Lazar, Forming functional fat: A growing understanding of adipocyte differentiation. *Nat. Rev. Mol. Cell Biol.* **12**, 722–734 (2011). doi: 10.1038/nrm3198; pmid: 21952300
9. R. Siersbæk, R. Nielsen, S. Mandrup, Transcriptional networks and chromatin remodeling controlling adipogenesis. *Trends Endocrinol. Metab.* **23**, 56–64 (2012). doi: 10.1016/j.tem.2011.10.001; pmid: 22079269
10. E. D. Rosen, O. A. MacDougald, Adipocyte differentiation from the inside out. *Nat. Rev. Mol. Cell Biol.* **7**, 885–896 (2006). doi: 10.1038/nrm2066; pmid: 17139329
11. K. E. Wellen et al., ATP-citrate lyase links cellular metabolism to histone acetylation. *Science* **324**, 1076–1080 (2009). doi: 10.1126/science.1164097; pmid: 19461003
12. J. R. Revollo, A. A. Grimm, S. Imai, The NAD biosynthesis pathway mediated by nicotinamide phosphoribosyltransferase regulates Sir2 activity in mammalian cells. *J. Biol. Chem.* **279**, 50754–50763 (2004). doi: 10.1074/jbc.M408388200; pmid: 15381699
13. Y. Li et al., Nicotinamide phosphoribosyltransferase (Nampt) affects the lineage fate determination of mesenchymal stem cells: A possible cause for reduced osteogenesis and increased adipogenesis in older individuals. *J. Bone Miner. Res.* **26**, 2656–2664 (2011). doi: 10.1002/jbmr.480; pmid: 21812028
14. X. Luo et al., PARP-1 controls the adipogenic transcriptional program by PARylating C/EBPβ and modulating its transcriptional activity. *Mol. Cell* **65**, 260–271 (2017). doi: 10.1016/j.molcel.2016.11.015; pmid: 28107648
15. H. Green, O. Kehinde, An established preadipose cell line and its differentiation in culture. II. Factors affecting the adipose

conversion. *Cell* **5**, 19–27 (1975). doi: 10.1016/0092-8674(75)90087-2; pmid: 165899

16. M. S. Rodeheffer, K. Birsoy, J. M. Friedman, Identification of white adipocyte progenitor cells in vivo. *Cell* **135**, 240–249 (2008). doi: 10.1016/j.cell.2008.09.036; pmid: 18835024

17. R. L. Van, C. E. Bayliss, D. A. Roncari, Cytological and enzymological characterization of adult human adipocyte precursors in culture. *J. Clin. Invest.* **58**, 699–704 (1976). doi: 10.1172/JCI108516; pmid: 956396

18. R. Siersbæk et al., Dynamic rewiring of promoter-anchored chromatin loops during adipocyte differentiation. *Mol. Cell* **66**, 420–435.e5 (2017). doi: 10.1016/j.molcel.2017.04.010; pmid: 28475875

19. R. Siersbæk et al., Extensive chromatin remodelling and establishment of transcription factor 'hotspots' during early adipogenesis. *EMBO J.* **30**, 1459–1472 (2011). doi: 10.1038/emboj.2011.65; pmid: 21427703

20. X. A. Cambronne et al., Biosensor reveals multiple sources for mitochondrial NAD⁺. *Science* **352**, 1474–1477 (2016). doi: 10.1126/science.aad5168; pmid: 27313049

21. M. F. Langelier, D. D. Ruhl, J. L. Planck, W. L. Kraus, J. M. Pascal, The Zn3 domain of human poly(ADP-ribose) polymerase-1 (PARP-1) functions in both DNA-dependent poly (ADP-ribose) synthesis activity and chromatin compaction. *J. Biol. Chem.* **285**, 18877–18887 (2010). doi: 10.1074/jbc.M110.105668; pmid: 20388712

22. Y. Sasaki, T. Nakagawa, X. Mao, A. DiAntonio, J. Milbrandt, NMNAT1 inhibits axon degeneration via blockade of SARM1-mediated NAD⁺ depletion. *eLife* **5**, e19749 (2016). doi: 10.7554/eLife.19749; pmid: 27735788

23. J. Yoshino, K. F. Mills, M. J. Yoon, S. Imai, Nicotinamide mononucleotide, a key NAD(+) intermediate, treats the pathophysiology of diet- and age-induced diabetes in mice. *Cell Metab.* **14**, 528–536 (2011). doi: 10.1016/j.cmet.2011.08.014; pmid: 21982712

24. Z. Liu, W. L. Kraus, Catalytic-independent functions of PARP-1 determine Sox2 pioneer activity at intractable genomic loci. *Mol. Cell* **65**, 589–603.e9 (2017). doi: 10.1016/j.molcel.2017.01.017; pmid: 28212747

25. M. V. Liberti, J. W. Locasale, The Warburg effect: How does it benefit cancer cells? *Trends Biochem. Sci.* **41**, 211–218 (2016). doi: 10.1016/j.tibs.2015.12.001; pmid: 26778478

26. R. H. Houtkooper, C. Cantó, R. J. Wanders, J. Auwerx, The secret life of NAD+: An old metabolite controlling new metabolic signaling pathways. *Endocr. Rev.* **31**, 194–223 (2010). doi: 10.1210/er.2009-0026; pmid: 20007326

27. M. Zaccolo, T. Pozzan, Discrete microdomains with high concentration of cAMP in stimulated rat neonatal cardiac myocytes. *Science* **295**, 1711–1715 (2002). doi: 10.1126/science.1069982; pmid: 11872839

28. M. F. Leite et al., Nuclear and cytosolic calcium are regulated independently. *Proc. Natl. Acad. Sci. U.S.A.* **100**, 2975–2980 (2003). doi: 10.1073/pnas.0536590100; pmid: 12606721

29. R. H. Wright et al., ADP-ribose-derived nuclear ATP synthesis by NUDIX5 is required for chromatin remodeling. *Science* **352**, 1221–1225 (2016). doi: 10.1126/science.aad9335; pmid: 27257257

30. V. Bulusu et al., Acetate Recapturing by Nuclear Acetyl-CoA Synthetase 2 Prevents Loss of Histone Acetylation during Oxygen and Serum Limitation. *Cell Rep.* **18**, 647–658 (2017). doi: 10.1016/j.celrep.2016.12.055; pmid: 28099844

31. K. E. Knockenhauer, T. U. Schwartz, The Nuclear Pore Complex as a Flexible and Dynamic Gate. *Cell* **164**, 1162–1171 (2016). doi: 10.1016/j.cell.2016.01.034; pmid: 26967283

32. H. Lee, W. C. DeLoache, J. E. Dueber, Spatial organization of enzymes for metabolic engineering. *Metab. Eng.* **14**, 242–251 (2012). doi: 10.1016/j.ymben.2011.09.003; pmid: 21946160

33. J. Ovádi, V. Saks, On the origin of intracellular compartmentation and organized metabolic systems. *Mol. Cell. Biochem.* **256**, 5–12 (2004). doi: 10.1023/B:MCBI.0000009855.14648.2c; pmid: 14977166

34. T. Zhang et al., Regulation of poly(ADP-ribose) polymerase-1-dependent gene expression through promoter-directed recruitment of a nuclear NAD+ synthase. *J. Biol. Chem.* **287**, 12405–12416 (2012). doi: 10.1074/jbc.M111.304469; pmid: 22334709

35. T. Zhang et al., Enzymes in the NAD+ salvage pathway regulate SIRT1 activity at target gene promoters. *J. Biol. Chem.* **284**, 20408–20417 (2009). doi: 10.1074/jbc.M109.016469; pmid: 19478080

36. P. M. Kekenes-Huskey, C. E. Scott, S. Atalay, Quantifying the Influence of the Crowded Cytoplasm on Small Molecule Diffusion. *J. Phys. Chem. B* **120**, 8696–8706 (2016). doi: 10.1021/acs.jpcb.6b03887; pmid: 27327486

37. J. L. Feldman et al., Kinetic and Structural Basis for Acyl-Group Selectivity and NAD(+) Dependence in Sirtuin-Catalyzed Deacylation. *Biochemistry* **54**, 3037–3050 (2015). doi: 10.1021/acs.biochem.5b00150; pmid: 25897714

38. J. E. Kim, J. Chen, Z. Lou, DBC1 is a negative regulator of SIRT1. *Nature* **451**, 583–586 (2008). doi: 10.1038/nature06500; pmid: 18235501

39. F. Picard et al., Sirt1 promotes fat mobilization in white adipocytes by repressing PPAR-gamma. *Nature* **429**, 771–776 (2004). doi: 10.1038/nature02583; pmid: 15175761

40. R. Mayoral et al., Adipocyte SIRT1 knockout promotes PPARγ activity, adipogenesis and insulin sensitivity in chronic-HFD and obesity. *Mol. Metab.* **4**, 378–391 (2015). doi: 10.1016/j.molmet.2015.02.007; pmid: 25973386

41. R. K. Gupta et al., Zfp423 expression identifies committed preadipocytes and localizes to adipose endothelial and perivascular cells. *Cell Metab.* **15**, 230–239 (2012). doi: 10.1016/j.cmet.2012.01.010; pmid: 22326224

42. M. Y. Kim, S. Mauro, N. Gévry, J. T. Lis, W. L. Kraus, NAD+-dependent modulation of chromatin structure and transcription by nucleosome binding properties of PARP-1. *Cell* **119**, 803–814 (2004). doi: 10.1016/j.cell.2004.11.002; pmid: 15607977

43. K. L. Meerbrey et al., The pINDUCER lentiviral toolkit for inducible RNA interference in vitro and in vivo. *Proc. Natl. Acad. Sci. U.S.A.* **108**, 3665–3670 (2011). doi: 10.1073/pnas.1019736108; pmid: 21307310

44. GTEx Consortium, The Genotype-Tissue Expression (GTEx) pilot analysis: Multitissue gene regulation in humans. *Science* **348**, 648–660 (2015). doi: 10.1126/science.1262110; pmid: 25954001

45. M. Kininis et al., Genomic analyses of transcription factor binding, histone acetylation, and gene expression reveal mechanistically distinct classes of estrogen-regulated promoters. *Mol. Cell. Biol.* **27**, 5090–5104 (2007). doi: 10.1128/MCB.00083-07; pmid: 17515612

46. R. Krishnakumar et al., Reciprocal binding of PARP-1 and histone H1 at promoters specifies transcriptional outcomes. *Science* **319**, 819–821 (2008). doi: 10.1126/science.1149250; pmid: 18258916

47. X. Luo, M. Chae, R. Krishnakumar, C. G. Danko, W. L. Kraus, Dynamic reorganization of the AC16 cardiomyocyte transcriptome in response to TNFα signaling revealed by integrated genomic analyses. *BMC Genomics* **15**, 155 (2014). doi: 10.1186/1471-2164-15-155; pmid: 24564208

48. S. Zhong et al., High-throughput illumina strand-specific RNA sequencing library preparation. *Cold Spring Harb. Protoc.* 10.1101/pdb.prot5652 (2011). doi: 10.1101/pdb.prot5652; pmid: 21807852

49. S. Andrews, FastQC (2015); www.bioinformatics.babraham.ac.uk/projects/fastqc.

50. D. Kim et al., TopHat2: Accurate alignment of transcriptomes in the presence of insertions, deletions and gene fusions. *Genome Biol.* **14**, R36 (2013). doi: 10.1186/gb-2013-14-4-r36; pmid: 23618408

51. C. Trapnell et al., Transcript assembly and quantification by RNA-Seq reveals unannotated transcripts and isoform switching during cell differentiation. *Nat. Biotechnol.* **28**, 511–515 (2010). doi: 10.1038/nbt.1621; pmid: 20436464

52. S. Wingett et al., HiCUP: Pipeline for mapping and processing Hi-C data. *F1000Res* **4**, 1310 (2015). pmid: 26835000

53. E. Yaffe, A. Tanay, Probabilistic modeling of Hi-C contact maps eliminates systematic biases to characterize global chromosomal architecture. *Nat. Genet.* **43**, 1059–1065 (2011). doi: 10.1038/ng.947; pmid: 22001755

54. A. R. Mullen et al., Reductive carboxylation supports growth in tumour cells with defective mitochondria. *Nature* **481**, 385–388 (2011). doi: 10.1038/nature10642; pmid: 22101431

55. T. Cheng et al., Pyruvate carboxylase is required for glutamine-independent growth of tumor cells. *Proc. Natl. Acad. Sci. U.S.A.* **108**, 8674–8679 (2011). doi: 10.1073/pnas.1016627108; pmid: 21555572

Science

Metabolic regulation of transcription through compartmentalized NAD$^+$ biosynthesis

Keun Woo Ryu, Tulip Nandu, Jiyeon Kim, Sridevi Challa, Ralph J. DeBerardinis and W. Lee Kraus

Integrating glucose and fat
Consuming too much glucose makes you fat, but it is unclear how this conversion is mediated by the body. Glycolysis links to gene transcription via the essential coenzyme nicotinamide adenine dinucleotide in its oxidized state (NAD$^+$). Ryu *et al.* found that compartmentalized NAD$^+$ synthesis and consumption integrate glucose metabolism and adipogenic (fat-promoting) transcription during adipocyte differentiation (see the Perspective by Trefely and Wellen). Competition between the NAD$^+$ precursors—nuclear NMNAT-1 and cytosolic NMNAT-2—for their common substrate, nicotinamide mononucleotide, regulates the balance between nuclear NAD$^+$ synthesis for adipogenic gene regulation and cytosolic NAD$^+$ synthesis used in metabolism.
Science, this issue p. eaan5780; see also p. 603

ARTICLE TOOLS	http://science.sciencemag.org/content/360/6389/eaan5780
SUPPLEMENTARY MATERIALS	http://science.sciencemag.org/content/suppl/2018/05/09/360.6389.eaan5780.DC1
RELATED CONTENT	http://science.sciencemag.org/content/sci/360/6389/603.full
REFERENCES	This article cites 57 articles, 18 of which you can access for free http://science.sciencemag.org/content/360/6389/eaan5780#BIBL
PERMISSIONS	http://www.sciencemag.org/help/reprints-and-permissions

Use of this article is subject to the Terms of Service